PERFORMANCE OF SHARK

SKIN INSPIRED MANUFACTURED

MODELS FOR SEPARATION CONTROL

by

JACOB CHASE PARSONS

AMY W. LANG, COMMITTEE CHAIR
JAMES P. HUBNER
DAVID W. MACPHEE

A THESIS

Submitted in partial fulfillment of the requirements
for the degree of Master of Science
in the Department of Aerospace Engineering and Mechanics
in the Graduate School of
The University of Alabama

TUSCALOOSA, ALABAMA

2020

ABSTRACT

The skin of fast-swimming sharks has been shown to have mechanisms able to reduce flow separation in both laminar and turbulent flows. This study analyzes arrays of bio-inspired microflaps and scales in a separated region generated by an adverse pressure gradient in a water tunnel environment. In the laminar boundary layer case, the microflap model bristles due to vortex interaction. This bristling controls the separation downstream of the model, reducing overall reversing flow by up to 59%. This investigation finds that the height of the protrusion into the boundary layer is an crucial factor in controlling the reversing flow. For the turbulent boundary layer, arrays of manufactured scales are tested in weak and strong adverse pressure gradients, controlled by a rotating cylinder. It has been found that the scales are ineffective at controlling separation in the weaker adverse pressure gradient case and increase the separation. However, in the stronger adverse pressure gradient conditions, the scales are highly effective at controlling separation, reducing the reversing flow by up to 70%. Additionally, the models are able to reattach the flow in extreme separation conditions.

LIST OF ABBREVIATIONS AND SYMBOLS

D	Diameter of cylinder
f	Rotation rate of cylinder
G	Gap distance between the cylinder and plate
I	Turbulence intensity
L	Distance from leading edge of plate to cylinder
L_T	Distance from leading edge of plate to wire trip
Re	Reynolds number based on characteristic length
S	Distance from cylinder to model array
U	Freestream velocity
α	Cylinder velocity ratio
δ	Boundary layer height
σ	Standard deviation
χ	Backflow coefficient

ACKNOWLEDGEMENTS

I want to thank my advisor and committee chair, Dr. Amy Lang, for making this research possible for the past several years. I also thank Dr. Paul Hubner and Dr. David MacPhee for offering their time to serve on my thesis committee. Leo Santos has been an excellent mentor since day one in the water tunnel facility, and I thank him for his guidance. Without Sean Devey's assistance in creating the bio-inspired models and Andrew Bonacci for his assistance in the lab and PIV flat plate data, this work would not be possible. I want to thank my parents for their support during my educational journey. Finally, I would like to thank my fiancée, Ashley, for her everlasting support in this endeavor even through the long hours and sacrifices made for this work.

CONTENTS

LIST OF TABLES

LIST OF FIGURES

CHAPTER 1: INTRODUCTION AND LITERATURE REVIEW

For decades, engineers have turned to nature to solve the most complicated problems in the field. One of these problems is flow separation, specifically in laminar and turbulent boundary layers, which has been a key area of research. There have been many active and passive separation control methods studied, but the passive methods are the primary focus of this review, as they are most relevant to the current study.

In incompressible flow over a body, there are three main types of drag: pressure drag, induced drag, and skin friction drag [1]. The present study focuses on pressure drag, which flow separation adversely effects. This phenomenon occurs in the presence of an adverse pressure gradient where low momentum fluid near the surface of the body travels upstream, in the opposite of the desired direction of travel. This causes a breakdown of the boundary layer which, when accompanied by an increase in the normal-to-wall velocity and a thickening of the rotational-flow region adjacent to the wall, causes adverse interactions with the free-stream flow [2]. This interaction is known as flow separation. Since flow separation is directly related to an increase in pressure drag, it is desirable to delay and reduce separation to reduce drag.

Separation behaves differently in laminar and turbulent flows. In laminar flow separation, the separation occurs along a spanwise line and the separation point is essentially constant over a period of time. However, this is not the case for turbulent flow separation, due to the natural fluctuations in turbulence. While this makes separation more difficult to quantify, a couple of key definitions can be used [2].

Simpson defines the point where the time-averaged wall shear stress is zero as the point of detachment [2]. This point was also shown to experience backflow 50% of the time, thus relating boundary layer separation to reversed flow. The percentage of time when a specific point experiences reversing flow is also referred to as the backflow coefficient, χ. A thesis by Gustavsson (1999) calculated χ and showed that $\chi = 0.50$ closely coincides with the line $U = 0$ [3].

To solve the problem of flow separation, researchers have studied nature's approach to flow control. A non-exhaustive list of biological samples investigated as a means of passive flow control include bird feathers [4,5], butterfly wings [6], fish fins [7,8], and shark denticles [9-12]. The bio-inspired surface in this study is the shark denticle, more specifically the denticles found on the flank region of the shortfin mako *Isurus oxyrinchus*.

Dermal denticles are found on the entirety of the shark's skin, primarily serving as natural armor for the animal [13]. The base of the denticle is anchored in the collagenous layer of the skin, known as the *stratum laxum*, while the hard enamel is exposed to water. On the crown of the majority of the mako's denticles are three small riblets oriented in the streamwise direction of the flow. The crowns of individual denticles interlock to make up the surface of the shark's skin [14]. Courtesy of Lang's 2015 study, Fig. 1.1 displays an up-close view of the mako shark skin.

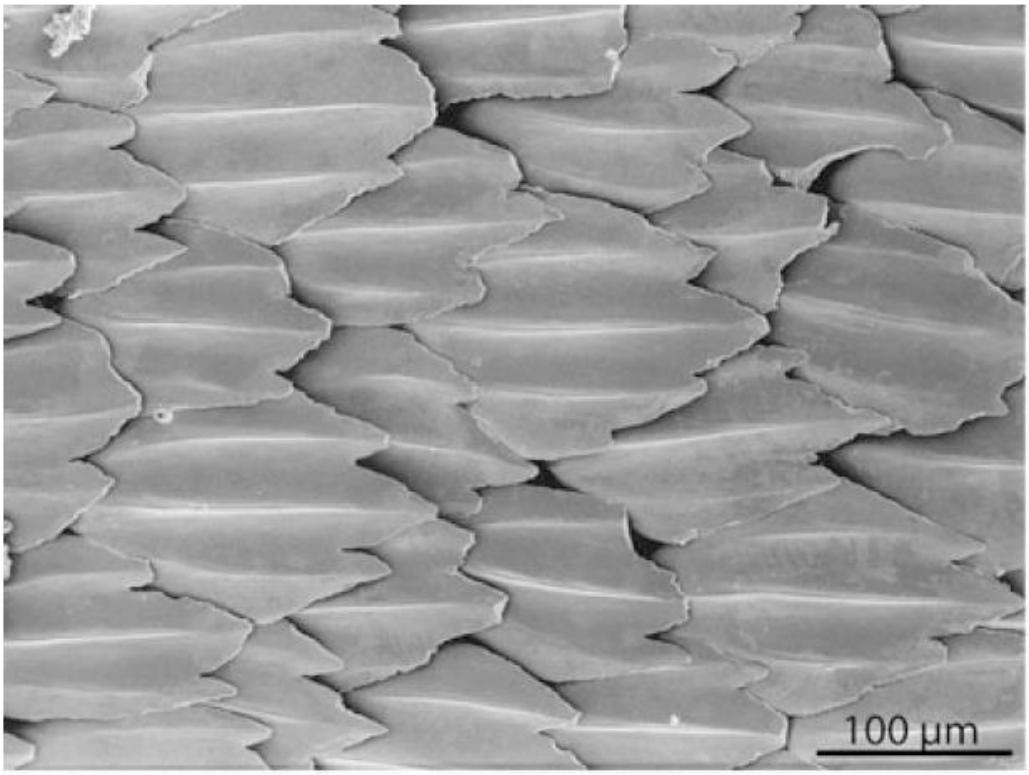

Figure 1.1 Scanning electron micrograph of the denticles on a shortfin mako shark [14]

In a 2012 study, Motta *et. al*. closely examined the morphology and flexibility of the dermal denticles on the shortfin mako shark *Isurus oxyrinchus* as well as the blacktip shark *Carcharhinus limbatus* [15]. The shortfin mako is the fastest known shark with recorded top speeds of up to 18.8 ms^{-1} (42 mph) [16], while the blacktip shark is a much slower swimmer, topping out at around 6.3 ms^{-1} (13 mph), which was measured during jumping [17]. The speed difference of the two sharks was critical to the study, as it was theorized that the scale morphology and flexibility would differ between the two specimens and it was thought that scales' ability to reduce drag on the shortfin mako would be a key factor in its high top speed. The study found that the shortfin mako shark has denticles with a relatively large crown and a small triangular base.

In contrast, the blacktip shark denticles have bases that are more rhomboid in shape with a smaller crown length to base length ratio. Additionally, the denticles on the blacktip shark are relatively constant on all regions on the shark. Notably, this was not the case with the shortfin mako specimen, as the base length-to-width ratio varied along the shark with the smallest value located in the flank region. The study found that the base geometry was indicative of the denticle flexibility because the greatest flexibility was recorded at the flank region. Fig. 1.2 shows a diagram of various locations on the shark with corresponding flexibility values. The region of interest applicable to the current study is the flank region, B2, where the bristling angle of the scales is approximately 50°, compared to a 30° bristling angle in the same region on the blacktip shark [15].

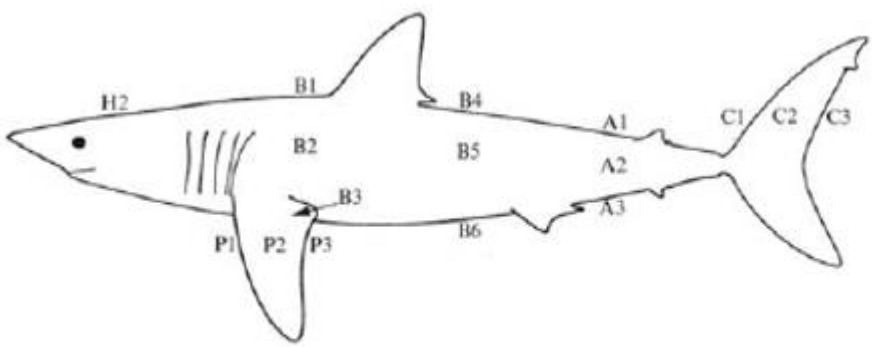

H2	$33^0 \pm 1$
B1	$28^0 \pm 1$
B2	$48^0 \pm 1$
B3	$30^0 \pm 1$
B4	$25^0 \pm 1$
B5	$43^0 \pm 2$
B6	$28^0 \pm 1$
A1	$25^0 \pm 1$
A2	$39^0 \pm 1$
A3	$16^0 \pm 3$
P1	$1^0 \pm 1$
P2	$23^0 \pm 1$
P3	$32^0 \pm 2$
C1	$25^0 \pm 2$
C2	$28^0 \pm 1$
C3	$30^0 \pm 2$

Figure 1.2 Measured scale bristling angles on the shortfin mako shark

The flank region is the area of maximum girth on the shark and where high curvature of the body will result from the lateral swimming motions, so it is expected that this region experiences the highest possibility of boundary layer separation and reversed flow. It has thus been theorized that the high scale flexibility in the region is a form of passive flow separation control where it is the most advantageous, assisting the shortfin mako shark in attaining high swimming speeds [15,18].

Motta *et. al.* also measured the crown and riblet sizes along with the riblet spacing. The crown is ~200 μm in length while the riblets have a height of ~30 μm and are spaced ~60 μm apart, which is relatively consistent along the shark's body. Fig. 1.3 shows a sample shortfin mako scale [15].

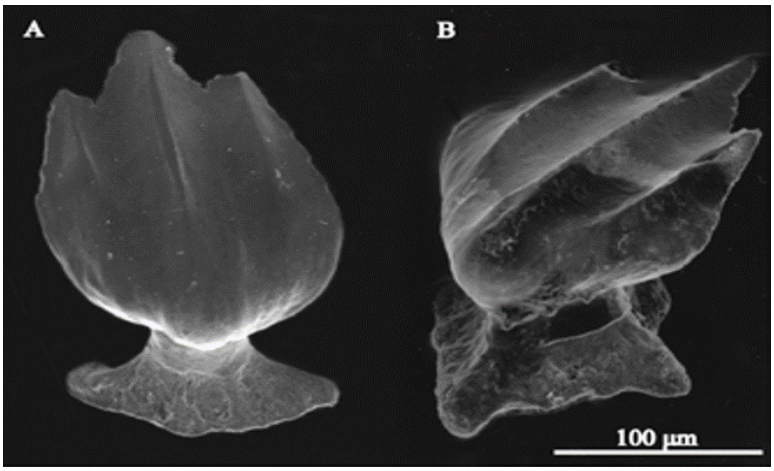

Figure 1.3 A shortfin mako shark scale viewed under an electron microscope

Due to their unique geometry, the denticles on the mako shark, especially the riblets, have been studied for their drag reduction potential since the mid-1980s [19-22]. While early studies were unable to efficiently produce a viable model for the shark scale itself, a riblet configuration inspired by the scales showed a skin friction drag reduction of 9% when compared to a smooth surface [20]. Bechert expanded on this study in 2000 by studying drag reduction on a

shark scale model with compliant scale anchoring [21]. This study investigated the skin friction reduction of the riblets and found only a 3% shear stress reduction compared to a smooth surface. This caused Bechert to introduce a new hypothesis that reversed flow could bristle the shark scales and the scales would then act as vortex generators. If the scales acted as vortex generators, this would induce mixing, thus delaying flow separation. Vortex generators protrude into the flow and must be placed upstream of separation points to be effective [23], which contradicts the theory that scales are bristled by reversing flow. It does not appear feasible that the shark can actively bristle scales upstream of the separation point, so this, along with supporting studies showing the ability for scales to be bristled via reversing flow downstream of the separation point [20,12], eliminates the possibility that the scales are behaving as vortex generators.

There are several studies of flow control methods that have relevance to the current investigation which should be considered, particularly the use of movable flaps placed close to the trailing edge of an airfoil. In one study, a bird feather-inspired flap was placed ~10% chord upstream of the trailing edge on the upper surface of an airfoil. The flap was allowed to passively actuate under laminar separation conditions and had a jagged edge, which was found to be more effective than a smooth trailing edge. The study also found the movable flap had a tendency to over-actuate beyond the optimal region of 60°-90°, which would cause the flow conditions to worsen [21]. The over-actuation of the flap, defined when the optimal bristling angle range is exceeded to an extent where the flaps worsen the flow conditions, is interesting to note since on the shortfin mako shark the bristling angle is physically limited to 50°, thus making over-actuation impossible. Building off this study, it was theorized that the shark scales work in a similar manner to the movable flaps but on a micro-scale level [9,10].

One might surmise that the actuation height of the movable flap relative to the boundary layer thickness is an important parameter for the effectiveness of flow control. Cases which are larger than the boundary layer, like bird feathers, may prove effective, but less intrusive geometries acting in the very low regions of the boundary layer, just as reversing flow is being initiated may be even more effective. A rough diagram of the operating regions in the boundary layer for bird feathers, vortex generators, and shark scales is shown in Fig. 1.4. For the feather inspired flap to be effective, the flap must be placed very close to the trailing edge of the airfoil and operates by extracting energy from the mean potential flow and can actuate beyond the boundary layer height [21]. Vortex generators operate closer to the surface with an effective operating range of 0.1δ – 0.5δ but must be located upstream of the separation point. Both bio-inspired flow control methods operate in the macro scale of the boundary layer. In contrast, the shark scales are effective in the lowest region of the boundary layer at ~0.1δ [15], operating on a micro level to control separation where it first develops.

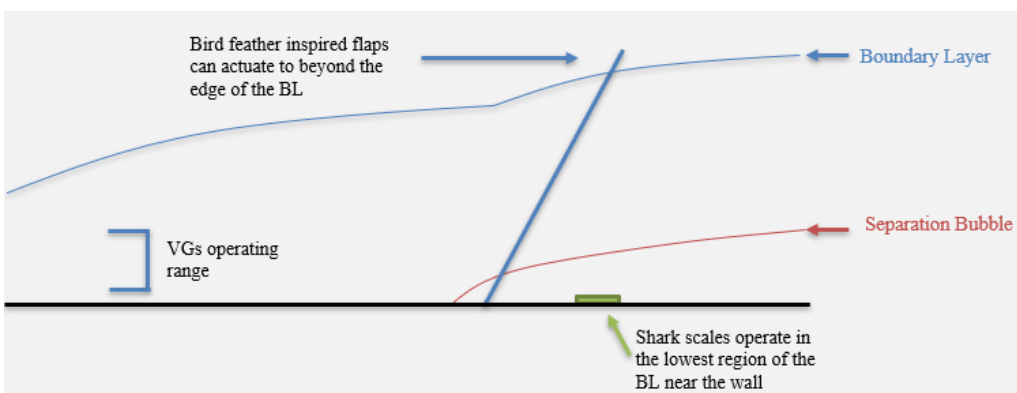

Figure 1.4 Diagram of passive flow control operating regions

There are also notable studies conducted with back-flow flaps in regard to dynamic stall control, including one where a 12.5% chord flap was placed at 30% chord downstream of the leading edge [24]. This flap was actively actuated and was allowed to passively actuate in a comparison case. The study found that the pitching moment peak was reduced by 25% for the

active flap case and by 19% for the passive flap case. This was accompanied by a 2.5% and 0.9% peak drag increase, respectively. The study also noted that the effectiveness of the flap was improved by tripping the boundary layer to turbulent, suggesting that the flap is better suited at higher Reynolds numbers [24]. Building off the previous study, the investigators focused on how the actively actuated flap would change the characteristics of the dynamic stall vortex. While the study did not find a notable effect on the flow separation over the airfoil, the most significant finding is that the flap split the dynamic stall vortex into two distinct vortex structures: one located upstream and one located downstream of the flap. Additionally, the vortex downstream of the flap was notably smaller compared to the case where the flap was closed. The difference in vortex size was theorized to be the cause of the 21% reduction in pitching moment peak found for the actively controlled flap compared to the case where the flap was closed [25].

In the current investigation, bioinspired surfaces based on the shortfin mako are used to study the passive flow control behavior during scale bristling under reversing flow conditions. This is not the first study to manufacture bioinspired surfaces based on the shortfin mako to investigate passive flow control. Outside of Bechert and his team's work in the late 1990s and early 2000s are two notable studies for shark scale inspired flow control. The first is a 2008 study by Lang *et. al.* where a manufactured model of the shark scales showed the formation of a partial slip condition close to the model compared to the no-slip condition found in the flat plate case for both laminar and turbulent boundary layer conditions. The formation of embedded vortices in the model was also observed [9].

Another notable study [26] investigated the pressure drop in channels in laminar and turbulent boundary layer conditions with various bioinspired surfaces, including a shark skin model. The study found that the reduction in drag for the shark skin model was much more prevalent in turbulent conditions compared to laminar conditions. The study found a pressure drop reduction of 30% compared to the smooth surface case for the turbulent boundary layer conditions, while a pressure drop reduction of only 12% was observed in the laminar flow case [26]. More recent studies on shark skin-inspired surfaces have produced promising results. A recent CFD study [27] investigated an airfoil with denticle models arranged in various arrays on the suction side of the airfoil. For all cases, the scale models were locked at a bristling angle of 15°. The study provided evidence for some drag reduction but also found increased lift near stall conditions. However, due to the static nature of the scale models in the study and the location upstream of the separation point, the scales simply acted as vortex generators by tripping the boundary layer. The results are comparable to traditional vortex generators [27]. A separate study [28] investigated the effects of a manufactured surface inspired by mako shark scales. Due to technological limitations, it is currently infeasible to accurately replicate a surface covered in shark denticles below an ~10:1 scale geometrically. Therefore, the researchers created a simplified surface using cylindrical pillars with a large top, nearly resembling the top of a golf tee. This surface was created at a 1:1 scale with the shark denticles and was manufactured using deep reactive ion etching. When compared to a smooth surface, the manufactured surface produced a 10% higher mean velocity near the surface [28], which is evidence of a partial slip condition, comparable to what Lang's study in 2008 found.

In Wheelus' 2015 dissertation, mako shark scale-inspired models were used in rows to study cavity formation when the shark scales were bristled [29]. This was a static model at a

deflection angle of 45° at a 100:1 scale. The study aimed to match the cavity Reynolds number, and consequently the model protruded into the boundary layer an order of magnitude more than would be found using a real shark skin specimen. This resulted in the laminar boundary layer case failing to show any sign of flow control in the vertical velocity profiles. However, the turbulent case displayed enhanced mixing near the surface caused by the scales, a key element in the previously proposed theories [9,21] regarding the methods of how shark scales can control flow separation [29]. Additionally, Wheelus conducted a Digital Particle Image Velocimetry (DPIV) study on the vortices found in the cavities. A consistent cavity vortex was found in both the laminar and turbulent cases, but the vortex was much less defined in the turbulent case. Another notable find is a slightly positive vertical velocity in the leading cavity in the turbulent case, so flow was travelling upward out of the cavity into the boundary layer, a sign of the mixing of fluid momentum.

For the manufactured bioinspired surfaces based on shark skin previously discussed, all investigations utilized a static model. However, this is not the case on a real shark since the denticles are able to dynamically bristle in reversed flow, proven via imaging in a recent study [12]. To date, the only study with a manufactured dynamic shark scale-inspired surface was a thesis submitted in 2017 [30]. In this investigation, biomimetic shark scales were manufactured with a 3D printer and an array of scales was tested in a low-speed wind tunnel. Testing demonstrated that a microflap array with simplified geometry and a manufactured biomimetic shark scale array demonstrated passive flow-actuated bristling in separation bubbles generated by a fence [30]. While this study was mostly a proof of concept, it is the first recorded investigation, known by the author, to demonstrate bristling manufactured scales.

While the current investigation focuses on biomimetic scales, it would not have been possible without the substantial work that previous researchers completed at the UA water tunnel facility. A thesis by Smith (2011) examined shark skin samples on a hydrofoil in tripped turbulent boundary layer conditions. The study analyzed the backflow region on the suction side of the hydrofoil at various angles of attack. At each condition, natural shark skin was compared to shark skin that was painted over to prevent bristling and any beneficial roughness. The study found that at lower angles of attack (< 12°), the shark skin had significantly adverse effects, as the separation was larger and occurred farther upstream than the painted scales. This was apparent for all velocities tested. However, drastically different results were found at an angle of attack of 16°. At this point, a significant reduction (~30%) in the magnitude and thickness of the separated region was observed for the natural shark skin case compared to the case with the painted scales. Due to the drastic difference in flow control performance, it was theorized that a key threshold exists which determines if the shark skin is advantageous to use or has adverse effects [31]. This threshold is most likely related to the strength of the adverse pressure gradient.

The theory that the strength of the adverse pressure gradient is critical for the shark skin to be effective as a method of passive flow control is again present in Bradshaw's thesis (2014). This study investigated a shortfin mako's pectoral fin and a shark skin sample on a circular cylinder in a laminar boundary layer. Similar to Smith's study, Bradshaw studied the natural shark skin and then painted the skin for a comparison case. Bradshaw found that at low angles of attack (< 6°), the differences in backflow over the painted and unpainted surfaces were relatively small. However, at an angle of attack of 8° and 12°, the separated region was reduced for the natural shark skin. Additionally, Bradshaw found that as the Reynolds number increased, the more effective the natural shark skin was at controlling the flow separation. This study is further

evidence for the existence of a bristling threshold for shark scales, dependent on the adverse pressure gradient [32].

Due to the demonstrated importance of the adverse pressure gradient strength and location for the bristling of shark scales, a controllable and consistent adverse pressure gradient is highly advantageous for the current study. In the dissertation by Afroz (2014), it was demonstrated that by using a circular cylinder with an axis of rotation parallel to the surface, one can generate a predictable and consistent adverse pressure gradient in both laminar and turbulent boundary layer conditions. The reversed flow necessary for the bristling of the mako shark scales and the bio-inspired models occurs in the low-momentum region of the boundary layer and is caused by the low-pressure region the cylinder generates upstream [33].

To determine if the cylinder produces unsteady wake effects in the measurement window, the cylinder velocity ratio, α, is used. This is Eq. 1 where D is the diameter of the cylinder and f is its' rotation rate (rps).

$$\alpha = \frac{\pi D f}{U} \qquad (1)$$

If α is greater than 2.0, then the cylinder wake will not affect the region investigated since the unsteady wake effects will direct away from the wall [34]. In the first experiment of the current study, the wake effects intentionally interact with the wall, but is not the case in the second investigation. Afroz also found that as α increases for a fixed gap distance, G, χ also increases.

Other properties of the separation bubble also change with respect to an increase in α, including an increase in the separation height and the separation point moving farther upstream. Additionally, as α increases, the turbulent boundary layer separation becomes more asymmetrical and the reattachment point is moved downstream. The coefficient of pressure at the cylinder also increases as α increases, which concludes that the adverse pressure gradient strength must also increase with α [33]. In a subsequent study, Afroz (2014) utilized the rotating cylinder to examine the ability of shark skin to control separation on a flat plate in a laminar and turbulent boundary layer. The separation bubble height and backflow magnitudes were significantly reduced for the shark skin samples when compared to the flat plate data. Additionally, it was found that the shark skin was once again more effective at controlling separation under stronger adverse pressure gradient conditions. But even in stronger adverse pressure gradient conditions, complete control of the separation was not achieved, which could be due to the fact that the testing took place at velocities much lower than actual swimming speeds of sharks where the surface may act more effectively.

The present study examines the effectiveness of manufactured models in laminar and turbulent separation conditions. To quantify the separation, $\chi \geq 0.5$ [2] is used. The body of the shortfin mako shark is covered in denticles which can bristle to a maximum angle of 50º in the flank region [15]. The flank region is where the highest possibility of boundary layer separation occurs, so it has been theorized that the denticle flexibility in this region is a form of passive flow separation control [15,18]. This theory is important to the present study, so the models tested are limited to the maximum bristling angle of the shark denticle. Each denticle has a complex geometry with riblets and a crown length of ~200 μm [15]. This geometry is reproduced on a larger scale for the models used in the turbulent boundary layer study, but a simplified

version is used in the laminar boundary layer study. The shark scales have been theorized to work in a similar manner to bird feather-inspired flaps on a micro-scale level [9,10] by impeding the reversing flow in the region. It is likely that the actuation height of movable flaps relative to the boundary layer thickness is an important parameter for the effectiveness of flow control. This relation is studied in both laminar and turbulent boundary layer separation in the present study.

Another theorized method of how the shark scales control the flow is by enhancing mixing near the surface [9,21,29]. This is studied in the turbulent boundary layer case via a Reynolds stress analysis. In a study examining shark skin on an airfoil, it was found that the shark skin was more effective at controlling flow in deep-stall conditions, a case of extreme flow separation [31]. This is studied in the present turbulent boundary layer study by comparing separation created by a weak and strong adverse pressure gradient. To generate a controllable adverse pressure gradient, a rotating cylinder is used upstream of the measurement window. By changing the cylinder velocity ratio, the strength of the adverse pressure gradient can be adjusted. The two factors are correlated and affect the properties of the separation bubble [33]. The cylinder velocity ratio is a critical factor in this study. Not only is this related to the strength of the adverse pressure gradient, but when $\alpha \leq 2.0$, the wake of the cylinder will interact with the boundary layer in the measurement window [34]. For the turbulent flow conditions, the wake is properly averted away from the wall, so there is no interaction with the boundary layer. However, for the laminar boundary layer conditions studied, the wake interaction occurs and is a driving factor in the bristling of the microflap models. This bristling is caused by a vortex likely formed due to interacting instabilities sourced in the cylinder wake and the flow impediment of the microflap model. This interaction produces vortices whose structures are affected by the bristling of the microflap arrays.

The inspiration for the vortex interaction component in Chapter 3 comes from the dynamic stall vortex. Dynamic stall is a complicated fluid mechanics problem directly related to flow separation. If dynamic stall cannot be fully prevented, then the negative consequences of the phenomenon should be suppressed as much as possible. Research utilizing actively and passively actuated flaps on an airfoil to dampen the dynamic stall vortex has been conducted with positive results [24,25]. The present study investigates the effectiveness of microflaps in suppressing an unsteady vortex, similar to how a dynamic stall vortex would interact with a surface after the dynamic stall vortex has been shed.

Additionally, Du Clos (2018) documented that a vortex can form between scales on natural shark skin and can bristle these scales even in the absence of reversing flow [12]. This was a special case in the study as there was only one occurrence in n=27 bristling cycles. The shark scales were able to bristle without reversing flow due to the vortex creating a negative pressure region just upstream of the scale, which then bristled the scale. The study also found evidence of bifurcating flow at the scale tip, which would cause a vortex to form just under the shark scale.

Chapter 4 analyzes arrays of bio-inspired scales in turbulent boundary layer separation without the influence of the cylinder wake. The importance of the adverse pressure gradient strength is a key topic in this chapter as this is a determining factor in the effectiveness of the models controlling flow separation. The final chapter concludes and summarizes the work.

CHAPTER 2: EXPERIMENTAL SETUP

2.1 EXPERIMENTAL FACILITY

The experiments are conducted in a modified version of the Rolling Hills Research Corporation's Eidetics Model 1520 closed circuit water tunnel. The test section is 274 cm in length and 76 cm in height. This modified version has a test section 120 cm longer than the normal version in order to grow the large boundary layer necessary for testing. To account for the growth of the boundary layer displacement thickness along the length of the test section, the test section width increases from 41 cm at the entrance to 44 cm at the exit. The tunnel utilizes a high-performance impeller to achieve a maximum free stream velocity of 0.6 m/s, but the maximum velocity for testing is 0.5 m/s to reduce wear on the electric motor driving the impeller.

In an effort to minimize flow turbulence, the tunnel has a porous plate with a honeycomb design immediately preceding three stainless steel screens in the inlet plenum chamber. The honeycomb structure acts as a flow straightener. According to manufacturer testing, this setup results in an average turbulence intensity of <1% in the test section at a freestream velocity of 0.30 m/s.

The tunnel is ideal for particle imaging since the front, bottom, and back sides of the test section are tempered glass. The top is open to the free surface. For imaging purposes, a black plexiglass flat plate is mounted vertically and runs the length of the test section. This plate is modular in construction so that panels can be interchanged in the measurement window. A

regular flat plate and a modified panel with a recessed area to mount a microflap assembly are both utilized in the current study. Attached to the upstream edge of the flat plate at the beginning of the test section, there is a leading plate with an elliptical nose. At the exit of the test section, there is a movable flap which is adjusted to ensure that there is a zero-pressure gradient along the length of the test section when the rotating cylinder is not present. Based on a water height of 24 in (61 cm), the flap is set to an angle of 13.5°. An image of the water tunnel facility is shown in Fig. 2.1.

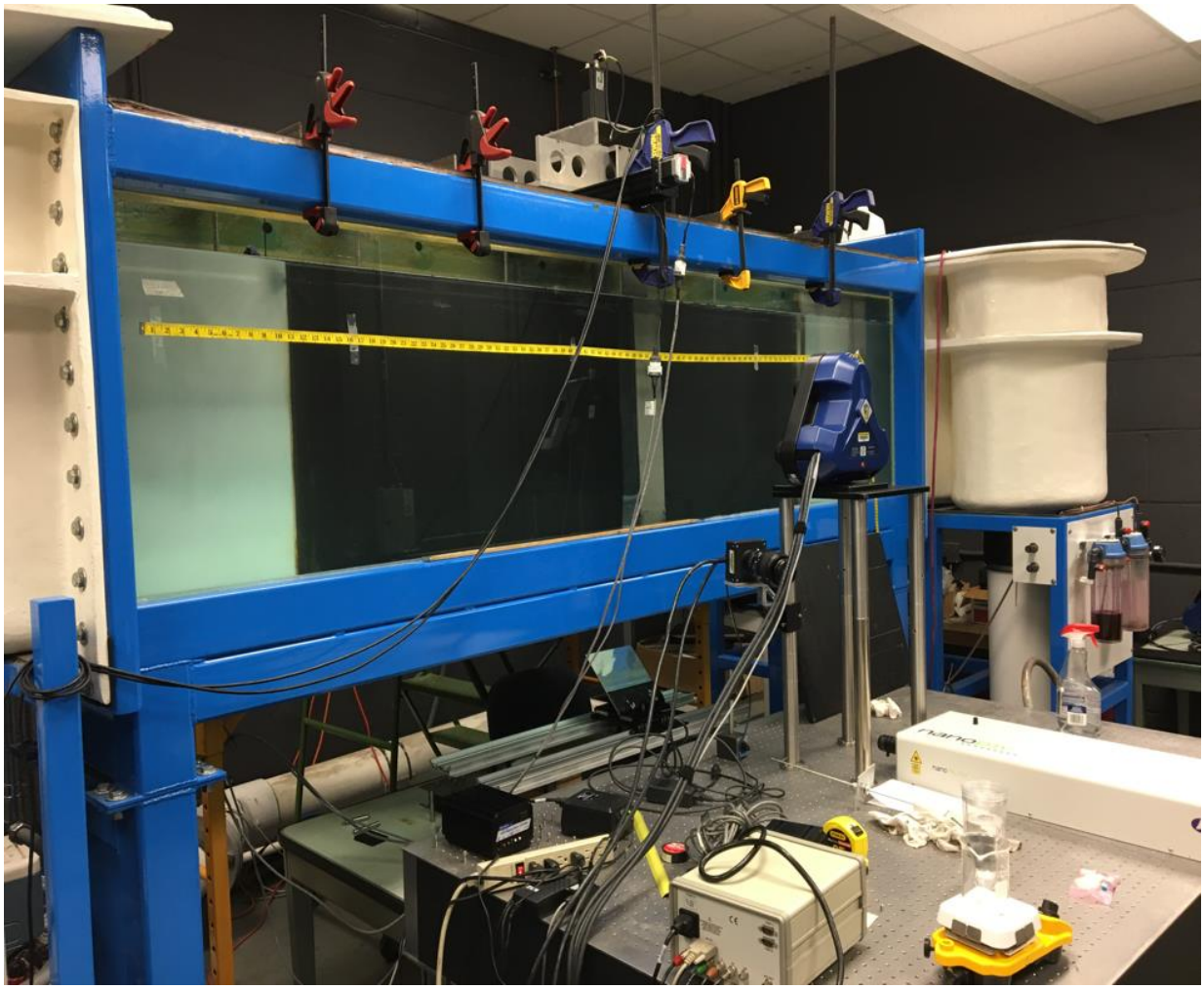

Figure 2.1 An image of the water tunnel facility

The reversing flow necessary for the present study, an adverse pressure gradient is required. A rotating circular cylinder is placed upstream of the measurement window to generate this adverse pressure gradient. Referring to the tunnel diagram in Fig. 2.2, the cylinder has a diameter of 5.1 cm and is placed 26.9D (137 cm) downstream from the leading edge of the flat plate. Additionally, the cylinder gap to the flat plate, G, is 0.78D (4 cm) for the laminar boundary layer case and 1.18D (6 cm) for the turbulent boundary layer case. The cylinder is located 1.86D (9.5 cm) upstream of the model array, which is centered in the measurement window. The cylinder rotates via a 3.0 N-m stepper motor mounted on the top and the rotation rate was varied for each of the three test cases in this experiment.

For the turbulent boundary layer separation experiment discussed in Chapter 4, a 3 mm diameter wire is inserted into the tunnel to trip the flow. This wire is on the surface of the flat plate perpendicular to the flow and is placed downstream of the leading edge at L_T = 8.24D (42 cm). Using this wire trip ensures a fully developed turbulent boundary layer [37].

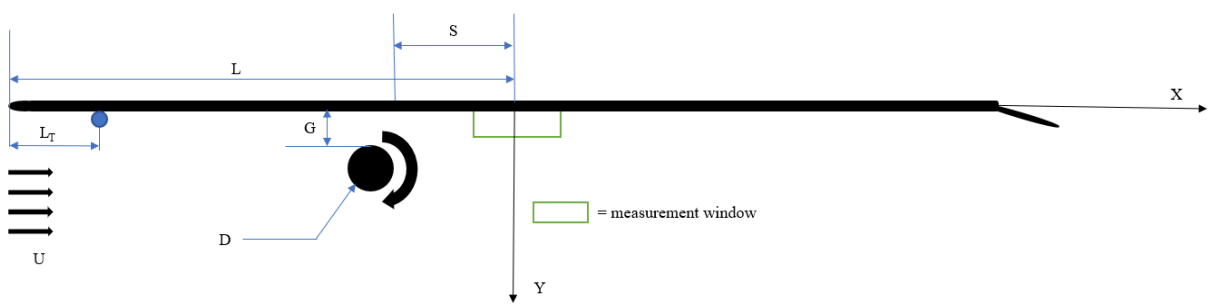

Figure 2.2 Experimental setup

2.2 IMAGE ACQUISITION AND ANALYSIS FOR PIV

The flow field is measured using a Digital Particle Image Velocimetry (DPIV) system. To accomplish this, the flow is seeded with 14 μm silver-coated hollow glass spheres and illuminated by a laser sheet generated by a Quatronix Darwin 30 mJ Nd:YLF laser. This laser runs at a frequency of 1.0 kHz at a beam wavelength of 527 nm. The laser sheet is obtained by passing the beam through a series of optics to produce a thin flat sheet. The beam is turned by 90° twice, passes through two Ø1" lenses, and is finally split into a sheet by a prism.

The images are captured using a MATLAB code which captures a total of 3000 frames in video format with a Basler A504k high speed camera at 1000 frames per second. Each image is 7 cm x 2.5 cm with a resolution of 1280 x 512 pixels. The images are processed using the Insight 4G software system and analyzed using Tecplot and MATLAB. To process an image in Insight 4G, the software must be properly calibrated by inputting the number of μm per one pixel in the image. For this experiment, the value was 83 μm/pixel which was calculated by taking a calibration image, shown in Fig. 2.3.

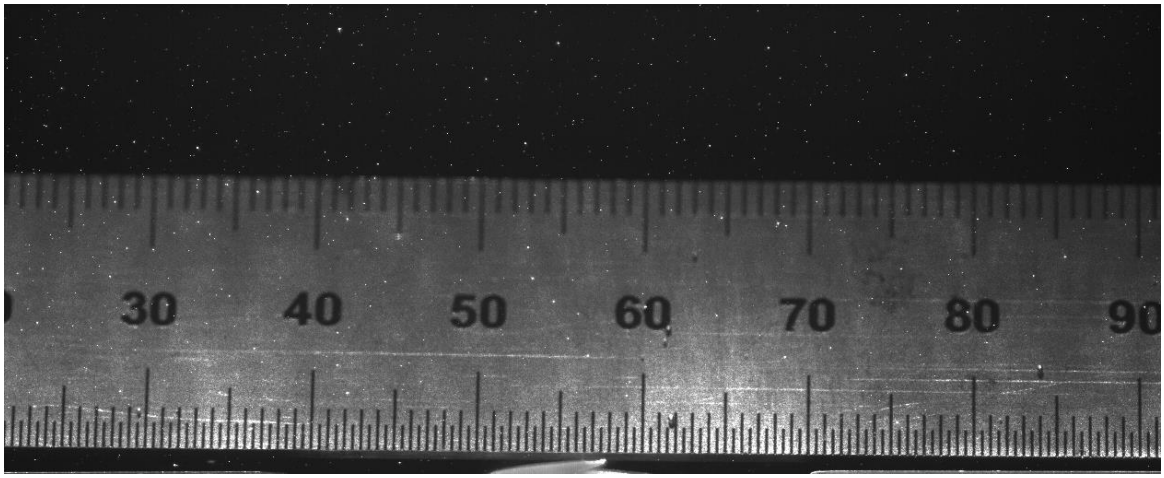

Figure 2.3 The calibration image

Both a static and dynamic processing mask are used to process the data. The static mask is standard to use on all DPIV data as it acts to crop the image, excluding errors on the border of the image. Since this experiment utilizes dynamic microflaps, a dynamic mask is also utilized. Relative to the surrounding flow field, the microflaps reflect more of the laser sheet, so the high brightness is masked out of the image to avoid the software improperly calculating the flow field near the model. Once the image is masked, it is passed through a pre-processor, which is an image calculator using subtraction so that the system examines two adjacent images and subtracts the particle positions to calculate the distance traveled for a specific particle. A recursive Nyquist grid is used to process the images as it offers the highest accuracy. Each image has at least two passes with this grid, which uses the positions of the previous pass for a more refined computation in subsequent passes. A pass is validated when the tolerance in velocity calculations is 2 pixels or less. An FFT Correlation Engine and a Gaussian Peak Engine were also used in the processing. Each pass begins in the top left of the image and runs to the bottom right. Since fine details are less important in the upper part of the image, the calculation area is 64 x 64 pixels to save computation time. Closer to the surface, where details are critical, the calculation area is 10 x 10 pixels, the finest resolution possible with this software. The image is finally passed through a post-processing filter to eliminate any bad vectors due to local insufficient seeding. Insight 4G gives a total percentage of good vectors for an image, which was 96% at a minimum, but were typically 98% good vectors. A ‘good vector’ is defined as a vector which passes the validation guidelines as previously discussed. In literature, it is accepted that for a laminar flow using DPIV, ≥ 95% of all vectors processed must pass the validation tolerance [36]. All images adhere to this guideline.

2.3 DATA ACQUISITION AND ANALYSIS FOR V3V

Due to the 3-D effects observed in turbulent boundary layer separation, it can be advantageous to use a Volumetric 3-Component Velocimetry (V3V) system over a traditional DPIV system to capture the 3-D flow field. This system is used for the study of the turbulent boundary layer in the current study. To visualize the volume measured, the flow is seeded with polyamid seeding particles, 50 μm in diameter. The particles are then illuminated using a dual-head pulsed Nd:YAG laser operating at 532 nm. Two 50 mm cylindrical lenses diverge the laser pulses to illuminate a volume approximately 120 mm x 120 mm x 50 mm. To capture the images, the V3V-8000 3D camera is utilized and is connected to a 610035 LaserPulse synchronizer. Both the camera and synchronizer are manufactured by TSI Incorporated. The camera acquires images at 15 fps using the Insight V3V 4G software system. The laser pulses have a staggered firing sequence and images are captured on each pulse. Thus, for one complete 3-D image, a total of six images are captured. To process the data, the Insight V3V 4G software compares the frames of each laser pulse to calculate the velocity between two points in 3D space.

The V3V system is unable to produce the same level of detail as DPIV primarily due to two reasons. The current V3V setup is designed for a more macro view of the flow compared to DPIV. This is evident by the DPIV-equivalent plane (perpendicular to the plate) being 70% larger for the V3V system. Additionally, the system accounts for the dimension parallel to the plate. Due to the large investigation volume, high pixel resolution cameras are used instead of high-speed cameras. While this is beneficial for macro observations, it is a drawback when, for instance, small turbulent flow structures near the surface are investigated. The second reason that V3V may not be as detailed as DPIV in some scenarios is due to the processing grid system. Unlike DPIV, the processing grid size cannot be changed depending on the location in the image.

In a V3V image, the total number of points where data is calculated along a directional axis can be four times less than in a DPIV image. The lower spatial and time accuracies discussed are direct consequences of the large investigation volume. Regardless of these drawbacks, the V3V system is sufficient for the scope of the current study.

2.4 2-D MICROFLAP MODEL

A simplified shark skin-inspired microflap model is used for testing in laminar flow conditions. The base of the microflap is designed to easily rotate if the bristling is initiated by reversing flow. Additionally, to simplify the geometry, and since they are not the focus of the present study, the riblets found on the mako shark scale [15] are removed. Other researchers in the UA water tunnel facility had previously attempted to use reversing flow to passively bristle a manufactured flap model but were unsuccessful. The span of the flap tested was 20 cm (3.92 D), which is likely the cause of the unsuccessful experiment. The bristling of shark scales occurs quickly on a micro level, at a viscous timescale of about 4 μs [12]. In relation to this, not all scales along the same span line will bristle at the same time since the bristling occurs in sporadic areas on the shark skin. Therefore, it is likely the backflow generated was not strong enough to actuate the original flap model. This resulted in a new microflap design which is 15% of the original size with a span of 3 cm (0.59D).

A key interest in the current study is if microflap size is an important factor in the flow control. Three chord lengths of 6 mm, 8 mm, and 10 mm are selected to be investigated. Assuming a normal swimming velocity for the shortfin mako shark of 10 m/s, a given denticle will protrude ~1.2% (0.012δ) into the boundary layer when bristled at 50° [34]. Though this protrusion height is not reproducible in the water tunnel, the microflap models can still be used to investigate the importance of the model's boundary layer protrusion height. The tested chord

lengths and their protrusion into the boundary layer at a bristling angle of 50° are compared to the natural shark scale in Table 2.1.

	Chord Length (mm)	**Protrusion Height (mm)**	**Boundary Layer Protrusion (%)**
Microflap 1	6.0	4.75	25.0
Microflap 2	8.0	6.13	32.0
Microflap 3	10.0	7.66	40.0
Shark Scale	0.20	0.15	1.25

Table 2.1 Boundary layer protrusion of microflap models and natural shark skin

The laminar Blasius estimation is used to calculate the boundary layer thickness for the microflaps and a turbulent estimation is used for the shark skin [37]. These equations are Eq. 2 and Eq. 3, respectively. For the laminar and turbulent flow cases in this study, minus the shark skin case, the location that this is calculated corresponds to the center of the model (27.4 x/D).

$$\delta_{\mathrm{lam}} = \frac{5\mathrm{L}}{\sqrt{\mathrm{Re_L}}} \qquad (2)$$

$$\delta_{\mathrm{turb}} = \frac{0.38\mathrm{L}}{\mathrm{Re_L}^{1/5}} \qquad (3)$$

This assumes that $\mathrm{Re_L} \approx 1.46 \times 10^5$ for the laminar case with zero pressure gradient and is calculated with respect to the leading edge of the plate. For the shark, $\mathrm{Re_L} \approx 5.0 \times 10^5$ [18]. It should be noted that as the laminar boundary layer is subjected to an adverse pressure gradient, it will significantly grow in height thus reducing the protrusion percentage within the boundary layer for the experimental conditions. The goal here is to vary the microflap chord length so the control effect, with respect to the protrusion into the boundary layer, can be studied. A side view of the microflap model is displayed in Figure 2.4.

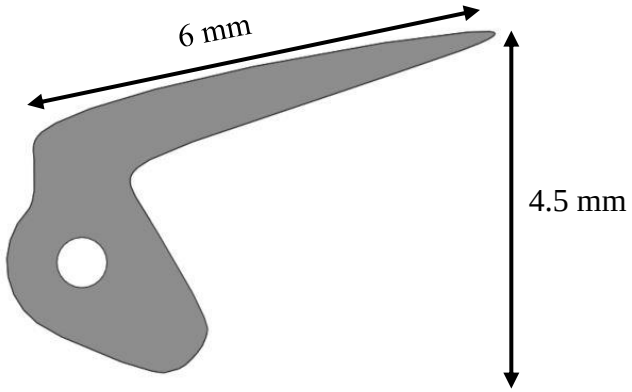

Figure 2.4 Side view of the microflap model

Since the skin of the shortfin mako shark is an array of overlapping scales, a small array of four microflaps is used for testing. Unlike the shark skin, there is no overlap in the spanwise direction for this array, only some small overlap in the chord direction, visible in Fig. 2.5 (a). Four microflaps are arranged in a 6 cm x 3 cm baseplate with a recessed area for the microflaps to slot into. The microflaps freely rotate on a 0.3 mm diameter wire which runs the entire span of the test assembly. To limit the bristling angle to 50°, small obstructions are printed on the interior ends of the recessed area. The entire assembly is constructed via a 3D printer using PLA plastic. Since the microflaps are placed in the tunnel perpendicular relative to the floor, there should be no body gravitational forces affecting the performance of the microflaps. A CAD render of the full test model assembly is shown in Figure 2.5.

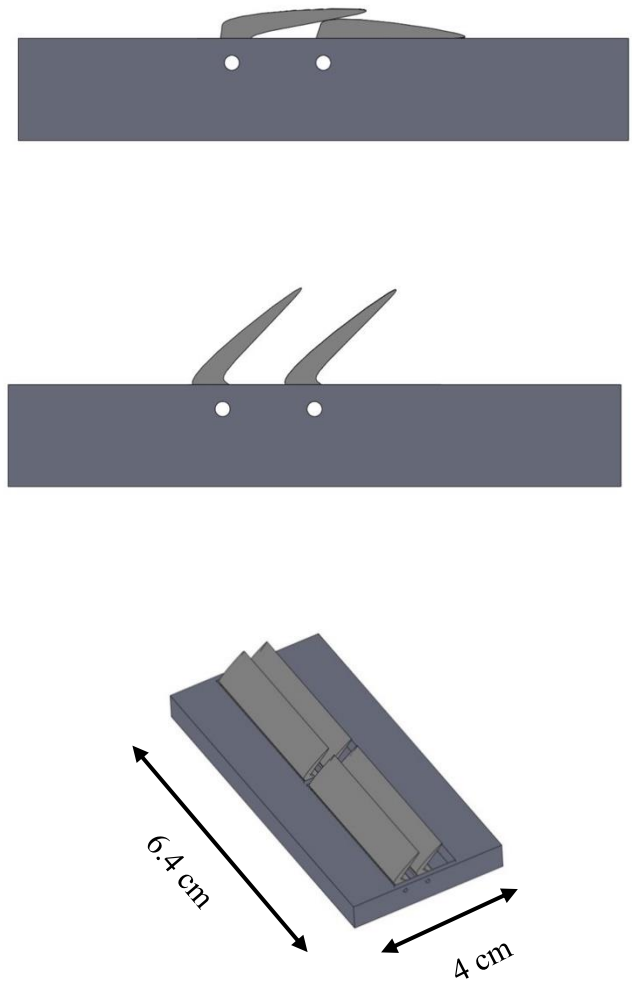

Figure 2.5 CAD rendering of model. a) unbristled, b) bristled, c) 3D view

2.5 BIO-INSPIRED SCALE MODEL

To better mimic the denticles of the mako shark to be tested in turbulent flow conditions, a new shark scale model is created. This model is a closer replica of the shark denticles with an accurate base width to crown ratio, riblets, and the three-point crown tip, similar to Fig. 1.3. As noted in literature, the bristling of the natural shark scales occurs in localized areas and happens rapidly [12], so not all scales on the same span line will bristle. Due to this, a new test model

assembly is designed in collaboration with a colleague. The original assembly is designed to house four rows of microscales, measuring 2 mm in chord length and 1.5 mm in width, totaling 22 scales. The design is then modified to add two more rows, increasing the total number of scales to 33. A 0.3 mm diameter wire is passed through the base of the scale, allowing it to freely rotate. The base of the scale is designed so it only makes contact with the bottom of the recessed area at a bristling angle of 50°, thus physically limiting the model to the natural bristling angle of the flank region on the mako shark. A rendering of the original scale size 1 model and an image of the scale size 2 model are shown in Figure 2.7. The scale size 2 is a model with larger scales, used as a comparison case. This second model has an array of three large scales, each with a chord length of 8 mm.

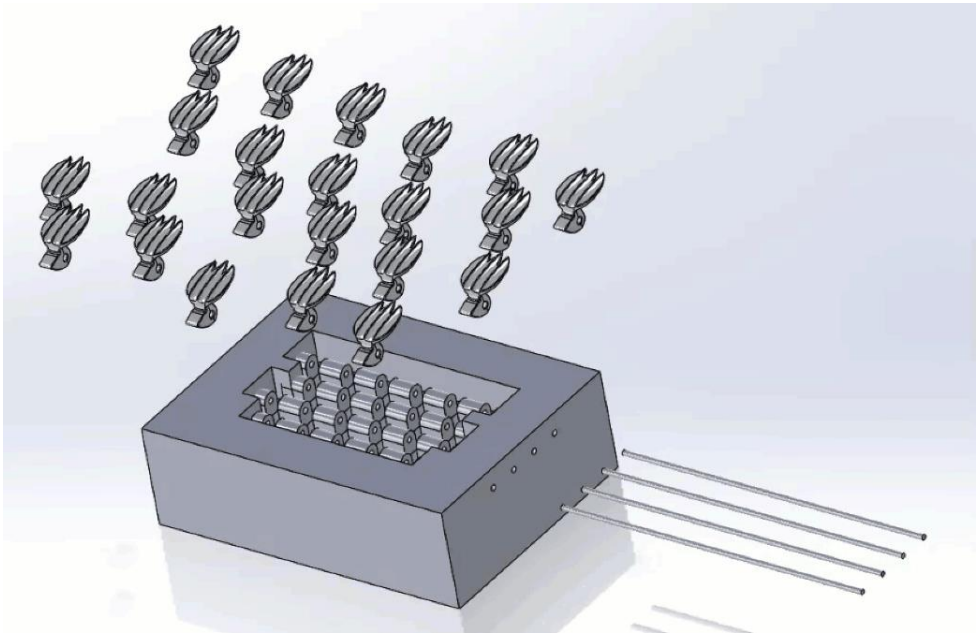

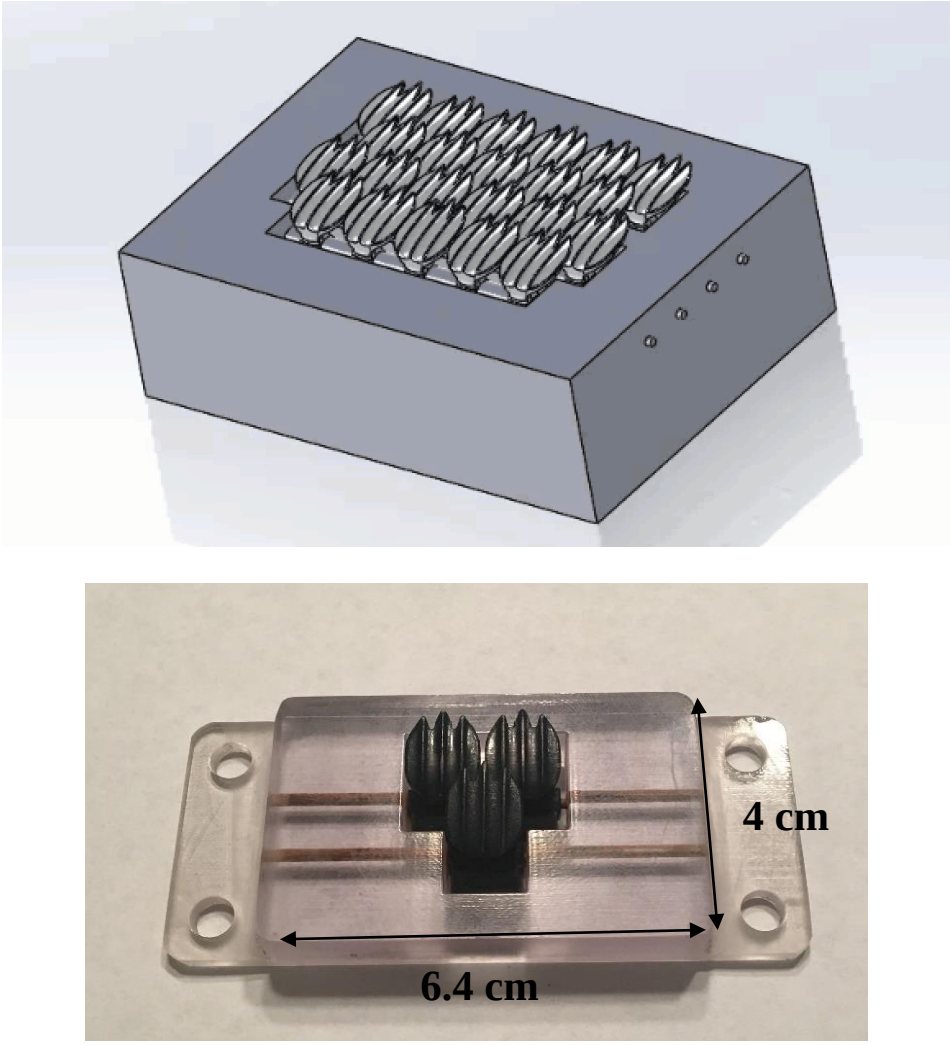

Figure 2.6 CAD Rendering of the original test model design in an expanded form (top), the full assembled model (middle), and an image of the scale size 2 model.

Similar to the previous experiment, the protrusion into the boundary layer is calculated for each scale size. The Reynolds number for each test case is calculated and used in the turbulent boundary layer thickness estimation to calculate the protrusion height, shown in Table 2.2. Scale 1 is the smaller, 2 mm chord scale and Scale 2 is the larger, 8 mm scale. Again, as the boundary layer is subjected to an adverse pressure gradient its height will grow significantly thus reducing the local scale height protrusion percentage within the boundary layer.

Tunnel Velocity (m/s)	**Reynolds Number**	**Boundary Layer Height (mm)**	**Scale 1 BL Protrusion (%)**	**Scale 2 BL Protrusion (%)**
0.33	4.82×10^5	40.6	3.8	12.3
0.40	5.85×10^5	39.1	3.9	12.8
0.47	6.87×10^5	37.9	4.0	13.2

Table 2.2 Protrusion height for TBL cases

CHAPTER 3: EXAMINING LARGE VORTEX INTERACTION WITH MICROFLAPS IN LAMINAR BOUNDARY LAYER SEPARATION

3.1 INTRODUCTION

The first study aims to demonstrate that manufactured microflaps, inspired by the denticles of the shortfin mako shark, are able to passively bristle by a vortex in a laminar boundary layer. This vortex forms upstream of the test models and is likely a result of the interactions of cylinder wake instabilities and the instabilities caused by the microflap models on the laminar separation bubble. The presence of the microflaps move the separation point upstream of the model and the wake instabilities cause the shedding of large vortex structures from the leading edge of the separation bubble, which is similar to a dynamic stall-type process. These types of vortex structures do not occur without the presence of the microflaps nor when the rotation rate of the cylinder is high enough to dissipate the wake ($\alpha \geq 2.0$). The study shows that the microflaps dynamically react to flow conditions to reduce the overall backflow and control separation. Finally, microflaps with differing chord lengths are compared to find which is most effective at controlling separation. For natural shark skin, the bristled scales protrude into the boundary layer ~1.5%, so the different sized microflaps are used to search for a correlation between protrusion percentage and separation control effectiveness.

3.2 OBSERVATIONS OF BRISTLING MICROFLAPS

The objective of this investigation is to confirm the passive bristling of microflaps by a vortex in a water tunnel facility. The images presented are captured using the tunnel setup in Fig. 2.2 with $Re_L = 1.46 \times 10^5$ and $\alpha = 0.53$, thus the wake of the cylinder affects the boundary layer within the measurement window. The microflap model used has a protrusion into the boundary layer of 0.25δ. Fig. 3.1 shows a sequence of DPIV images demonstrating an example of a vortex causing the microflap models to bristle. Each vector represents velocity and the size corresponds to the respective magnitude. The freestream flow moves from left to right. Fig. 3.1 (a) shows a clear vortex on the flat plate upstream of the microflap models. Fig. 3.1 (b) shows the vortex on the model array with the microflaps near the maximum bristling angle. Downstream of the microflap array, some rotational flow of the vortex is impeded by the downstream microflap. This impediment causes the vortex to lose much of its definitive structure, as seen in Fig. 3.1 (c). Fig. 3.2 offers a more general view of the flow field with a clear vortex upstream of the microflaps in Fig. 3.2 (a) and the disorganized remnants of this vortex in Fig. 3.2 (b). Fig. 3.2 (a) and Fig. 3.1 (a) are the same image, as is the case with Fig. 3.2 (b) and Fig. 3.1 (c). In addition to the DPIV image examples of a bristling cycle for the 0.25δ protrusion height microflap, the number of bristling cycle occurrences for the three microflap sizes is recorded. For the same conditions outlined for the DPIV images, a total of seven runs of 3,000 images each are acquired for each microflap size. This corresponds to a total of 21 s of data for each microflap. Over the entire data set, n = 60 bristling cycles are observed for an average of 0.95 bristling cycles per second. Each microflap size records 20 unique bristling cycles, so the frequency of bristling cycles does not depend on the model's boundary layer protrusion height in this limited sample.

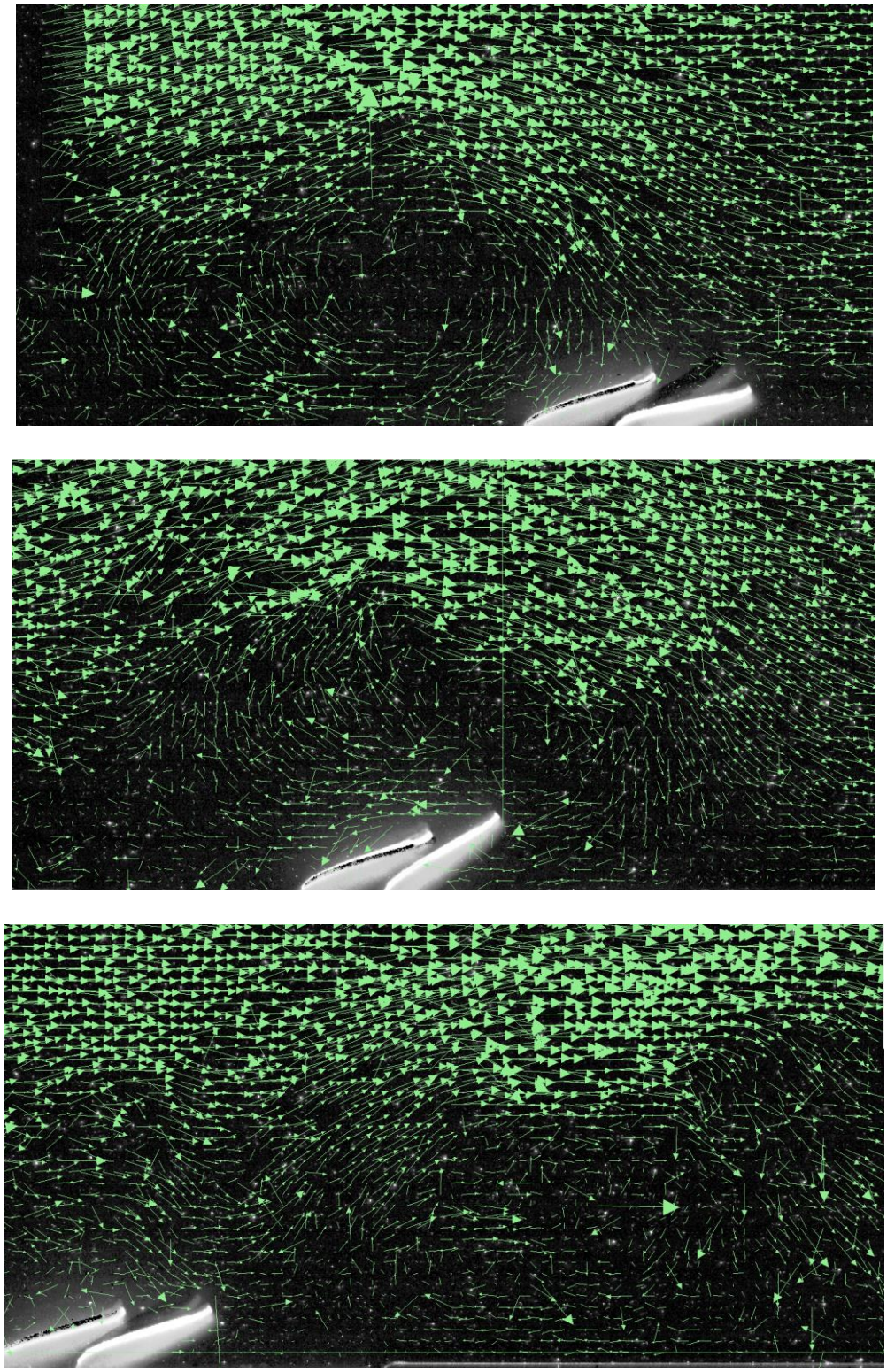

Figure 3.1 DPIV images of a vortex bristling the microflaps. a) t = 0 ms, b) t = 205 ms, c) t = 435 ms

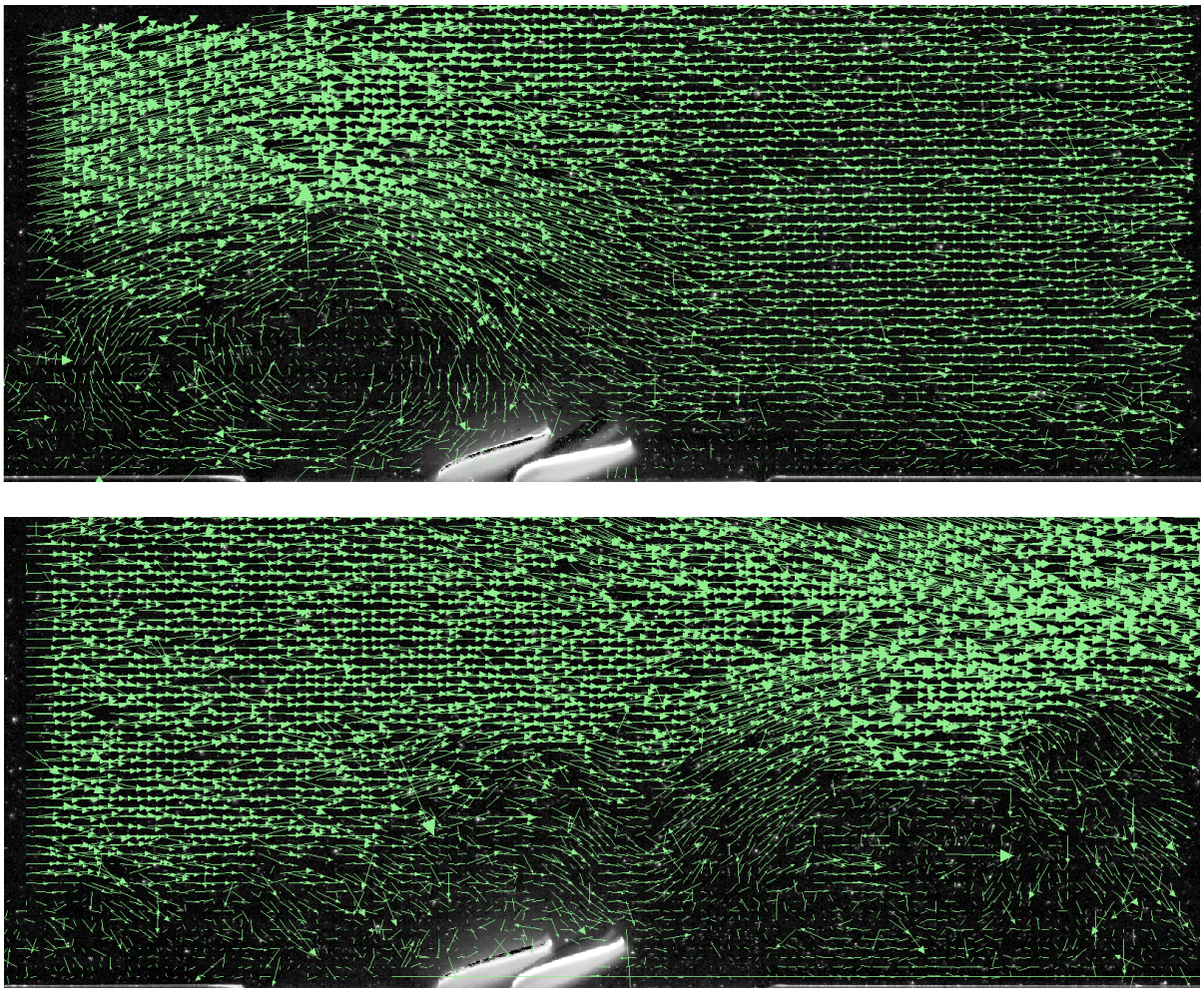

Figure 3.2 Full flow field view at a) t = 0 ms, b) t = 435 ms

The duration of each bristling cycle is also recorded and the average cycle duration for the microflap sizes is compared to the duration for a natural shark scale. This is recorded in Table 3.1.

	Bristling Cycle Duration (s)
Microflap 1 (0.25δ)	0.428 ± 0.089
Microflap 2 (0.32δ)	0.445 ± 0.021
Microflap 3 (0.40δ)	0.489 ± 0.033
Shark Scale (0.015δ)	$1.7 \times 10^{-3} \pm 8.0 \times 10^{-4}$

Table 3.1 Bristling cycle duration comparison

Compared to the natural shark scale [12], the bristling cycle duration of the microflap models is two orders of magnitude longer. As a comparison between microflap models, the average duration for each size is within one standard deviation, so the results are inconclusive. Outside of statistical error, a possible explanation for this data is the extra material used for the larger microflaps. This extra material increases the mass of the microflap, so the vortex would have more difficulty overcoming the inertia of the microflap, thus extending the bristling cycle. One note is a single outlier in the data set, a special case observed as a bristling cycle for microflap 1 (0.25δ). For this case (no data presented), the center of the vortex did not approach the microflap array as closely as the other cases. As a result, the bristling cycle duration is significantly longer than all other cases at 0.625 s, which is > 2σ from the average for the 0.25δ protrusion height data set.

3.3 MICROFLAP-VORTEX INTERACTIONS

In section 3.2, it is shown that a vortex, likely originating from instability interactions between the cylinder wake and microflap model, travels downstream and interacts with the test model which bristles the microflaps. The purpose of this experiment is to conduct an investigation of the interaction between this vortex and the microflaps. The three different sized microflaps are each tested at three flow conditions and compared to flat plate data, originally

collected by a colleague. The rotation rate of the cylinder is the only flow variable altered between test cases. The test conditions are found in Table 3.2.

U	0.1 m/s
Re_L	1.46 x 10^5
α_1	0.40
α_2	0.48
α_3	0.53

Table 3.2 Flow parameters for the laminar boundary layer cases

For each set of data, seven runs of 3,000 images are acquired with the camera set at 1,000 fps. The seven runs are then time-averaged to produce velocity contour plots. Streamlines have been selected as an overlay on the contour plots in an attempt to map the location and size of vortices. For the microflap cases, the center of the array is on the flat plate located at 28.7 x/D. The microflaps are dynamically bristling in each case, as shown in section 3.2, by interacting with a vortex as it moves downstream. On average, the microflaps undergo a bristling cycle every 0.95 s, so each run has an average of three bristling cycles. Fig. 3.3 displays the time-averaged results for case 1, $\alpha = 0.40$. For the plots, the white box marks the location of the microflap array.

The red arrow marks the theoretical height (0.38 y/D) of the laminar boundary with no adverse pressure gradient at 28.7 x/D. The blue arrow marks the point of maximum deflection (50°) for each microflap model. These values are found in Table 3.3.

	Protrusion Height (y/D)
Microflap 1 (0.25δ)	0.09
Microflap 2 (0.32δ)	0.12
Microflap 3 (0.40δ)	0.16

Table 3.3 Maximum bristling height for the microflap models

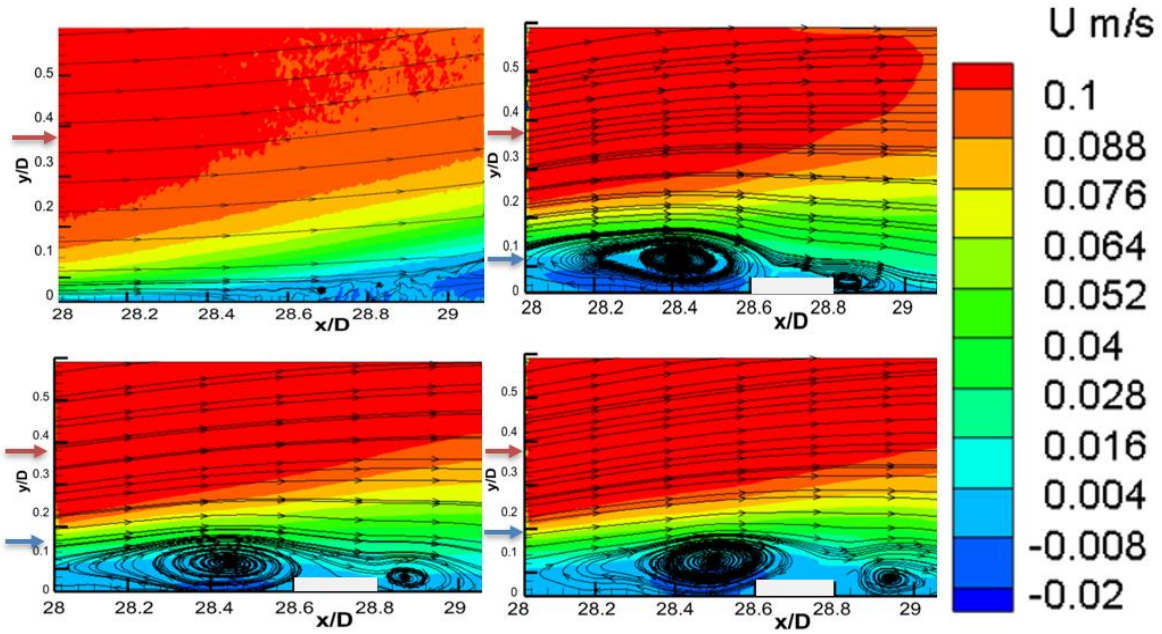

Figure 3.3 Velocity contour plots: case 1. a) flat plate, b) 0.25δ , c) 0.32δ, d) 0.40δ

The flat plate data for case 1 shows the steady growth of the boundary layer with pockets of reversing flow near the wall at 29.0 x/D. Comparing the test models to this, a similar boundary layer growth is apparent, but the magnitude of the reversing velocity downstream of the test models is less than that of the flat plate. There is a more intense region of reversed flow upstream of the test models, caused by the impediment of flow in the preferred direction by the microflaps. For the 0.32δ and 0.40δ protrusion cases, the upstream vortex has a similar height to the microflap maximum bristling height, suggesting that these two factors are correlated. Downstream of the models another vortex is present and is notably smaller than the upstream vortex by ~50%. This vortex seems more dependent on the protrusion into the boundary layer. For the 10 mm flap (protrusion ~0.40δ), a vortex height of 0.11 y/D is present, while for the 6 mm flap (protrusion ~0.25δ), the vortex height is 0.05 y/D. Additionally, the former vortex center is ~13% farther downstream than the latter. The two cases with the smaller protrusion heights (0.25δ and 0.32δ) show a less than 3% difference in size and location of the downstream vortex.

The strength of the adverse pressure gradient is increased for case 2 with α=0.48. The results of this case are displayed in Fig. 3.4.

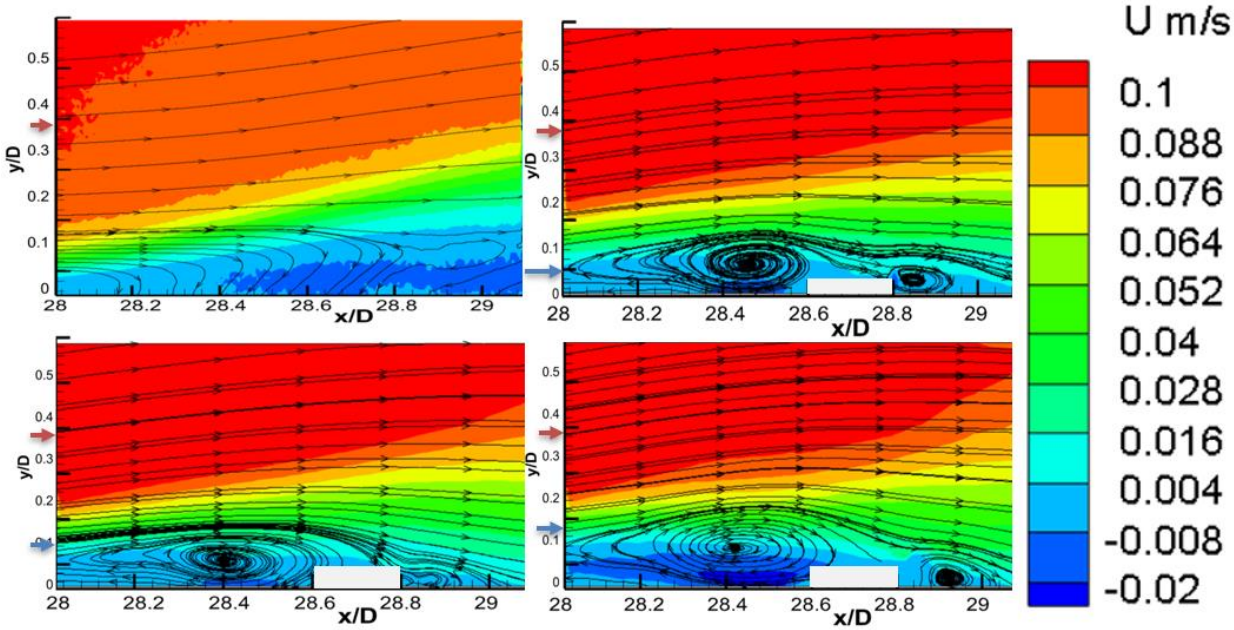

Figure 3.4 Velocity contour plots: case 2. a) flat plate, b) 0.25δ , c) 0.32δ, d) 0.40δ

Compared to case 1, the stronger adverse pressure gradient in case 2 produces a larger separation region where the significant reversing flow (dark blue contour) begins 60% farther upstream. As for how this affects the test models, similar general trends are evident between case 1 and case 2. Both cases have two vortical structures, a large structure upstream and a smaller structure downstream of the microflaps. However, there is a difference in the middle protrusion size 0.32δ. In case 1, the results for the two smaller protrusions are similar, but in case 2 there is a lack of a well-defined vortex core downstream of the microflaps. Some rotation is present, but not as defined as the largest and smallest protrusion sizes. It appears that the 0.25δ and 0.40δ protrusion sizes are similar downstream of the model since the vortex size difference is less than 3% and the location is 9.7% further downstream for the 0.40δ protrusion case.

For case 3, the adverse pressure gradient is increased further so that α=0.53. The results are shown in Fig. 3.5.

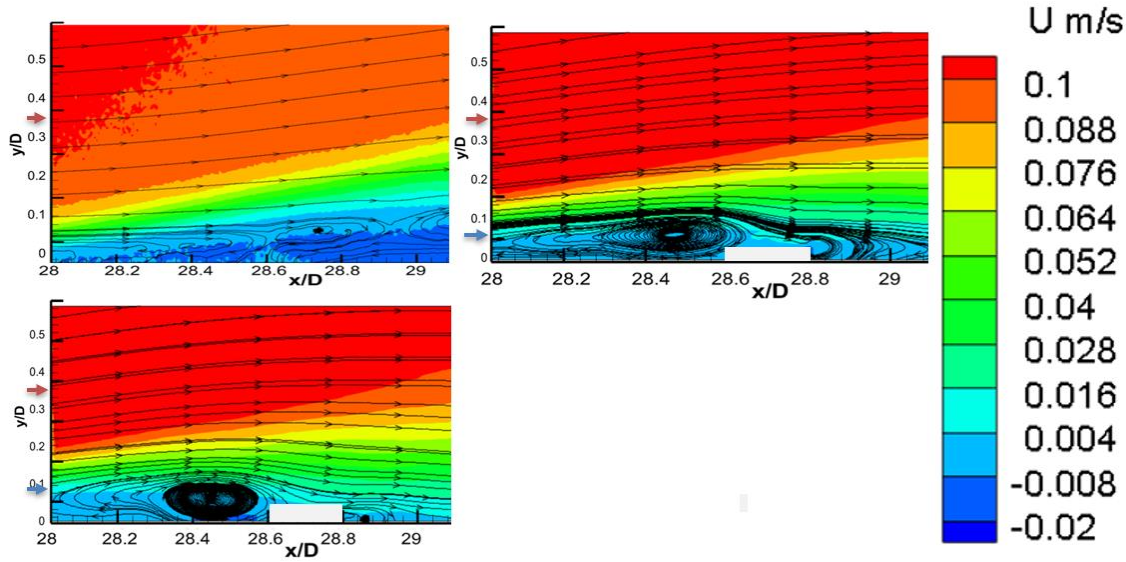

Figure 3.5 Velocity contour plots: case 3. a) flat plate, b) 0.25δ , c) 0.32δ

The increase in the adverse pressure gradient strength causes the formation of general vortical structures in the separation bubble. The strong regions of reversed flow are present throughout the entirety of the measurement window, though the height of the separated region is similar to case 2. As for the test models, the protrusion heights of 0.25δ and 0.32δ both show a clear vortex structure upstream of the microflaps, but the structure downstream is not as defined. The results for the protrusion case of 0.40δ have been omitted due to significant errors in the data.

In all three cases, the split in vortical structures is an intriguing finding for the relation to prior literature. In a 2017 study, Wolf *et. al.* examined the dynamic stall flow topology when an actively controlled backflow flap was used on an airfoil. The study found that when the dynamic stall vortex (DSV) for a deep stall case encountered the flap, the flap suppressed the backflow caused by the DSV immediately downstream. This suppression split the DSV into two smaller vortices, one in front and one behind the flap. The study found that this DSV split reduced the pitching moment peak by 21% but found no influence on the lift force or flow separation. A similar study in light stall characteristics [24] found that a backflow flap could break up the DSV into two smaller vortices, one located upstream and one downstream of the flap. The study found reductions in the pitching moment peak; however, this study also found a reduction of the reversed flow along the airfoil surface, but the significance of this on the reduced pitching moment peak was inconclusive.

The vortex observed in the present study is obviously not a DSV, but it is still a vortex in the flow interacting with a surface. The microflap models have shown evidence of breaking down this vortex into smaller vortical structures, located one upstream and one downstream of the microflaps on average. The similarities are intriguing and warrants further investigation. Due to the findings from Gardner (2017) the backflow flap reduced flow reversal [25] and the general interest of the biomimetic models reducing flow reversal, the backflow coefficient for the three cases are analyzed.

3.4 SEPARATED FLOW CONTROL

The backflow coefficient for the cases is calculated and plotted. Only the separated flow ($\chi \geq 0.5$) is plotted for clarity. Fig. 3.6 displays the results for case 1 ($\alpha = 0.40$).

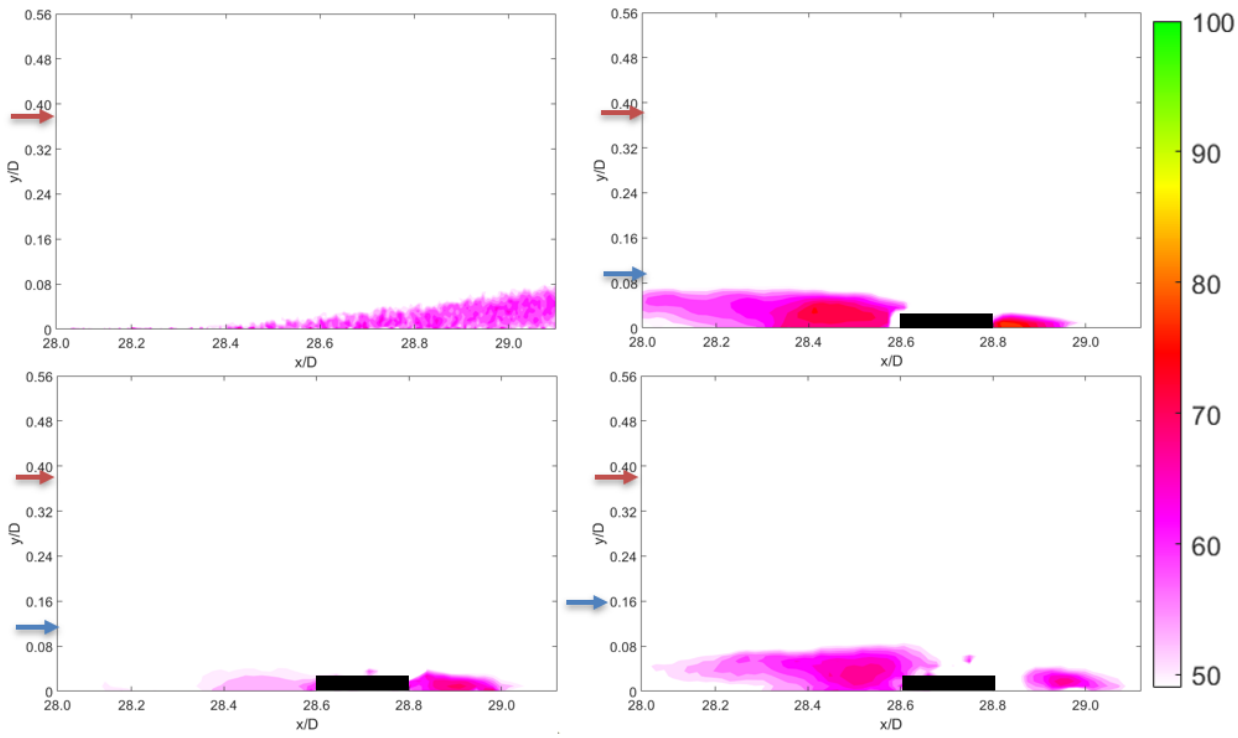

Figure 3.6 Reversing flow percentage: case 1. a) flat plate, b) 0.25δ , c) 0.32δ, d) 0.40δ

As expected, there is a larger percentage of reversing flow upstream of the microflaps due to flow being inhibited in the preferred direction. Though for investigating the reduction of reversed flow, the area of greatest interest is downstream of the microflaps. Immediately downstream, all cases exhibit separation. The smallest protrusion height (0.25δ) shows the smallest height of separation (0.03 y/D) but has the greatest backflow coefficient ($\chi = 0.8$). All three microflap cases display control of the reversed flow since separated flow on the flat plate case occurs downstream of 29.0 x/D with a height up to 0.08 y/D.

For the two smaller protrusion heights, there is no separated flow at or downstream of 29.0 x/D. For the 0.40δ protrusion height, some separation occurs at 29.0 x/D, but the height is ~33% less than the flat plate condition.

For the increased adverse pressure gradient in case 2, the results are displayed in Fig. 3.7.

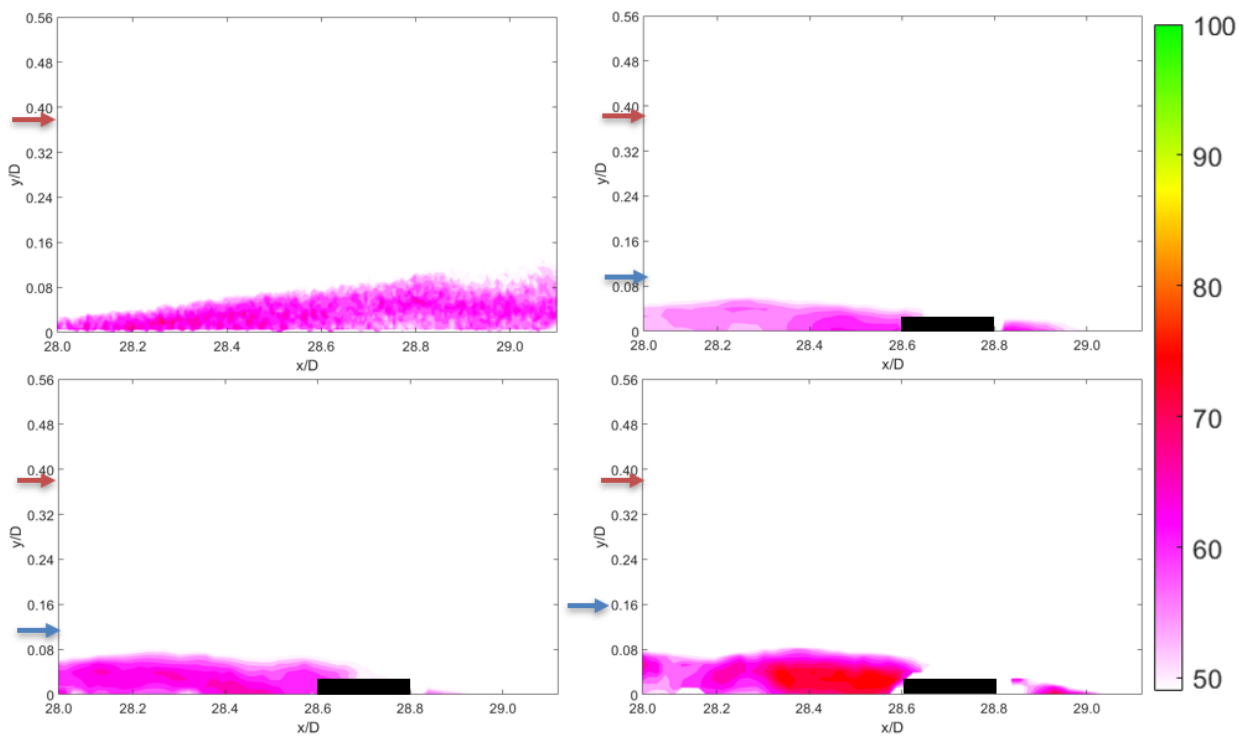

Figure 3.7 Reversing flow percentage: case 2. a) flat plate, b) 0.25δ , c) 0.32δ, d) 0.40δ

Comparing the flat plate conditions for case 1 and case 2, it is apparent that the separated flow in general is more prevalent in case 2, though the height of the separation bubble is the same in both cases (0.08 y/D). Similar to the case 1 results, the microflap models exhibit a significant degree of flow control. Unlike case 1, the three protrusion heights produce similar results to each other at 29.0 x/D, and the flow reattaches just downstream of 29.0 x/D for the 0.25δ and 0.40δ protrusion height case.

In the prior experiment with the vortex interactions, the protrusion height of 0.32δ did not produce a well-defined vortex structure downstream of the microflaps unlike the other two conditions. This observation translates to the present backflow study since the backflow is nearly eliminated in this area.

Case 3 increases the strength of the adverse pressure gradient (α = 0.53). Fig. 3.8 shows the results of this case.

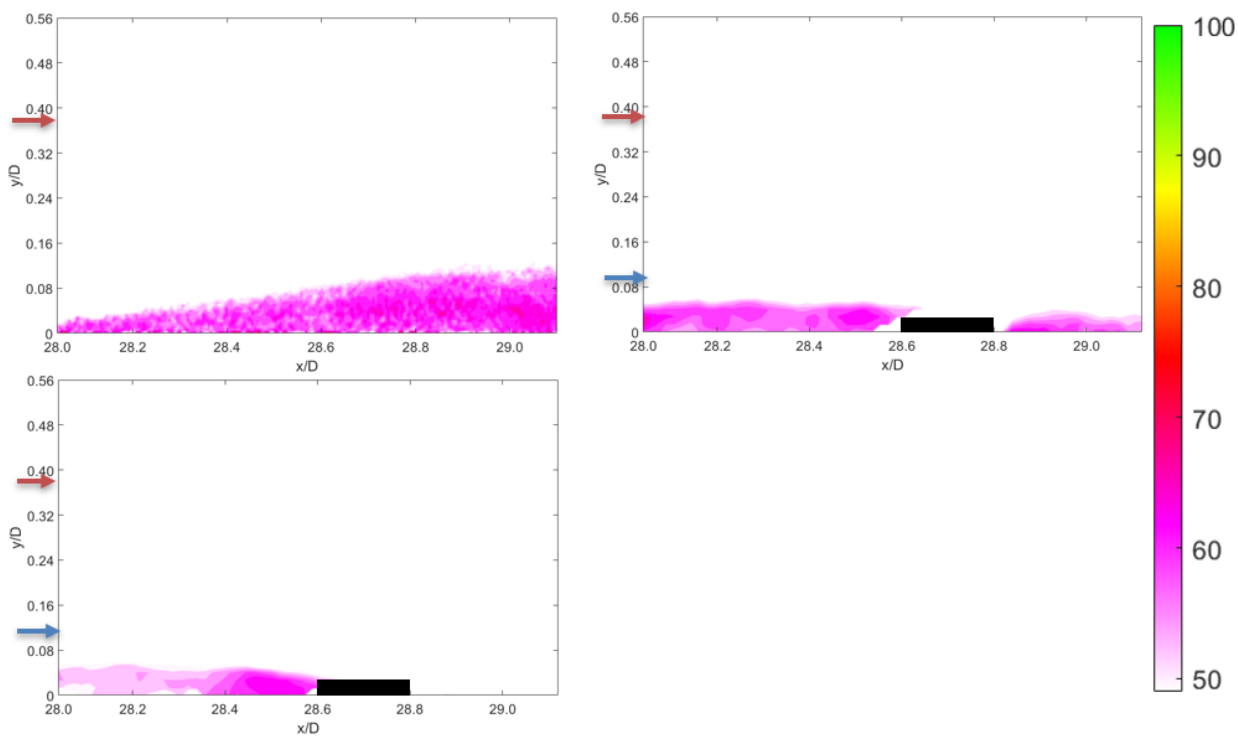

Figure 3.8 Reversing flow percentage: case 3. a) flat plate, b) 0.25δ , c) 0.32δ

For this stronger adverse pressure gradient, the height of the separation bubble for the flat plate condition increases by 25%. However, the microflap models again demonstrate excellent separation control downstream of the models with the 0.32δ protrusion case eliminating the separated region while also reducing the separated flow upstream of the microflap array.

As for the 0.24δ protrusion case, the maximum separation bubble height is reduced by 75%. As previously stated, the 0.40δ protrusion case is omitted due to significant data error.

3.5 WEIGHTED BACKFLOW

To better quantify the effectiveness of the microflap models at reducing reversing flow, a weighted area analysis is performed. Each reversing flow plot is split into a 104 x 203 grid. The area of each grid was multiplied by the backflow coefficient and summed. The weighted backflow coefficient (WBC) for all laminar boundary layer cases are shown in Table 3.4.

α	**Flat Plate WBC**	**0.25δ WBC**	**0.32δ WBC**	**0.40δ WBC**
0.40	1.24	0.81	0.51	1.09
0.48	1.58	0.90	1.12	1.44
0.53	1.86	1.03	0.71	

Table 3.4 Weighted backflow coefficient for LBL cases, Re = 1.46 x 10^5

The percent change relative to the flat plate case for each microflap model is shown in Table 3.5.

α	**0.25δ WBC**	**0.32δ WBC**	**0.40δ WBC**
0.40	-34.7%	-58.9%	-12.1%
0.48	-43.0%	-29.1%	-8.9%
0.53	-44.6%	-61.8%	

Table 3.5 Percent change in WBC for the microflap models, Re = 1.46 x 10^5

With the weighted backflow coefficient analysis, each case can be easily compared. Each model size successfully exhibited flow control with the 0.40δ protrusion height being the least effective at reducing the reversing flow. As for the two smaller models, the 0.25δ height reduced reversing flow by an average of 40.7% and the 0.32δ model reduced reversing flow by 49.9%.

Additionally, the models appear to be effective as α increases. The weighted backflow coefficient applies to the entire image, so a significant portion of the total backflow is located upstream of the microflap models. This reversing flow upstream of the model is the cause of the 0.32δ outlier for the $\alpha = 0.48$ case.

3.6 IMPORTANCE OF DYNAMIC BRISTLING

To demonstrate the importance of the dynamic bristling motion to the demonstrated separation control, the previous experiment was repeated with $\alpha > 2.0$ to eliminate the wake effects of the cylinder [34]. With wake effects suppressed, a source of flow instability was eliminated and the vortex observed in section 3.2 travelling downstream while interacting with the microflaps did not occur. Therefore, throughout the entire run, the microflaps were static in a semi-bristled state (~20°). This case is at $Re = 1.46 \times 10^5$ and $\alpha = 2.02$ and is shown in Fig. 3.9.

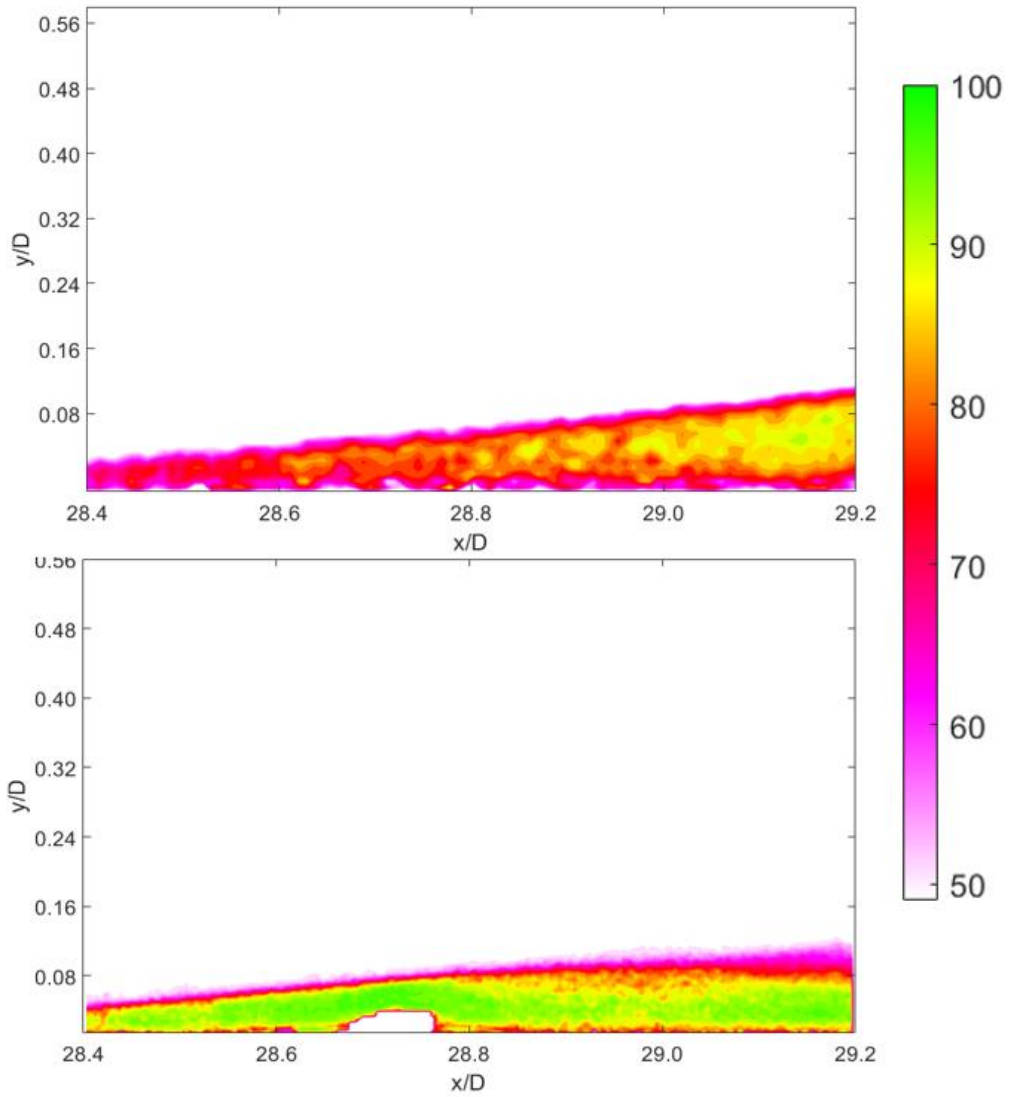

Figure 3.9 Static bristled case. a) flat plate, b) 0.25δ microflap model centered at 28.7 x/D.

This case shows that the flap does not dynamically bristle without the flow instabilities created by the cylinder wake interacting with the measurement window. There are no instances of a vortex travelling downstream near the plate, as was consistently present in the previously discussed cases. Using a WBC analysis, the WBC for the flat plate is 1.93 and is 5.76 for the microflap condition. This results in a 198% increase in reversing flow for the microflap case compared to the flat plate case. This concludes that the flow control does not occur without dynamic motion.

3.7 TURBULENCE INTENSITY

To demonstrate that the flow conditions are indeed laminar, the turbulence intensity for the three cases is shown in Fig. 3.10. Turbulence intensity is the root-mean-square of the turbulent velocity fluctuations by the mean velocity, as seen in Eq. 4.

$$I = \frac{\sqrt{\frac{1}{3}(u_x'^2 + u_y'^2}}{\sqrt{U_x^2 + U_y^2}} \tag{4}$$

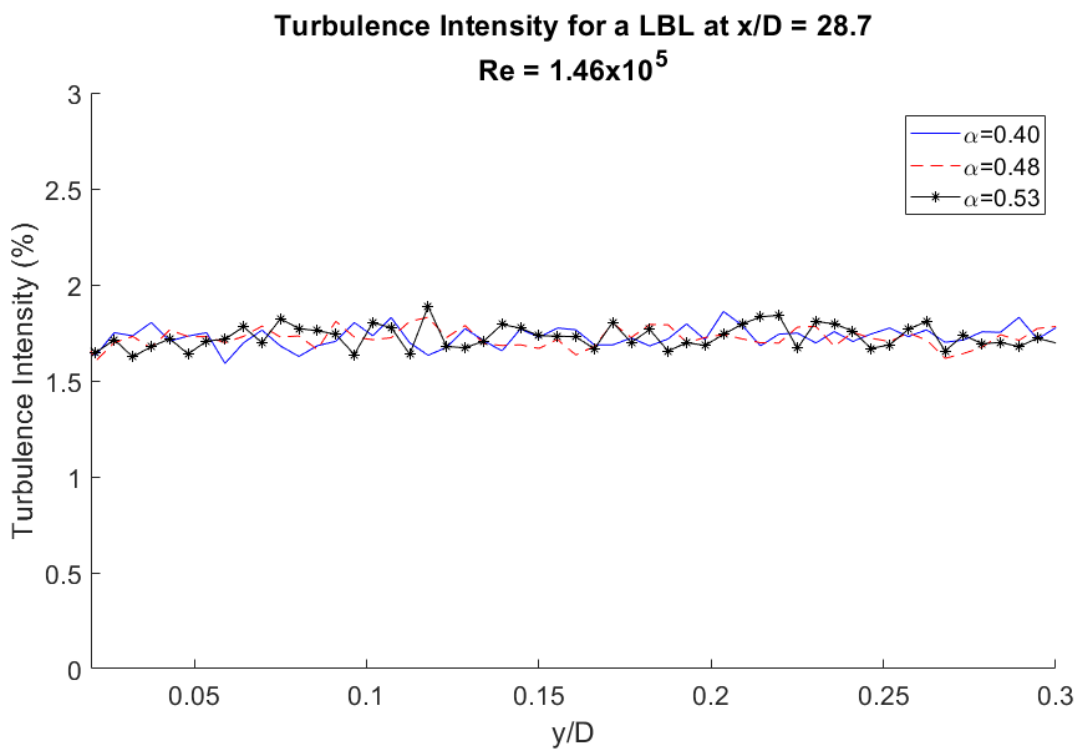

Figure 3.10 Turbulence intensity for the laminar boundary layer

In a water tunnel, a laminar flow will typically have a turbulence intensity of less than 2% [39]. This criterion is met in all three laminar cases in the present study.

3.8 CONCLUSIONS

This is the first known study to successfully bristle microflaps in a water tunnel environment. This is accomplished by allowing the wake of the rotating cylinder to affect the measurement window. This causes flow instabilities which, when combined with the instabilities created by the microflaps impeding the flow, form vortical structures. This vortex moves downstream along the plate, eventually interacting with the microflaps, causing them to bristle. This bristling impedes the rotational flow on one side of the vortex, which causes the vortex structure to break down. While the vortex is not completely suppressed, the integrity of the main structure of the vortex is compromised. Similar interaction has been noted in previous studies [24,25] when back flow flaps demonstrated an ability to break down a dynamic stall vortex and controlled flow separation. Due to the similarities of the studies, microflaps with respect to dynamic stall vortex interaction requires further investigation

A total of n = 60 bristling cycles have been recorded, which averages to a bristling cycle occurring every 0.95 seconds. The microflap sizing had no effect on this cycle frequency. In addition to the number of cycles, the duration of each bristling cycle is recorded. The duration is two orders of magnitude longer than the bristling cycle of a shark scale, which is to be expected. This investigation finds that the microflap size, and thereby protrusion height, does not significantly change the duration of the bristling cycle.

The velocity contours with an overlay of streamlines is analyzed for three cases of differing adverse pressure gradient strengths. This analysis finds two time-averaged vortical structures present in the flow, one upstream and one downstream of the microflap model array. The upstream vortex is larger and is caused by the microflaps impeding advancing flow.

The downstream vortex is smaller and is likely caused by the bristled microflaps impeding instances of reversing flow and redirecting it to the preferred flow direction.

The reversing flow percentage for each case is calculated and plotted. Each microflap model size exhibited flow control downstream of the array. Upstream of the array, a large region of reversing flow is present due to the models inhibiting flow in the preferred direction. To quantify the degree of separation control, the weighted backflow coefficient is used. The backflow coefficient at a point is multiplied by a non-dimensional differential area and summed. The result of this analysis finds that the 0.40δ is the least effective, reducing reversing flow by an average of 10.5% while the 0.25δ and 0.32δ cases reduce reversing flow by 40.7% and 49.9%, respectively. Therefore, the protrusion height is a significant factor in these cases. The maximum height of the uncontrolled reversed flow region is 0.28δ, so it is possible that this result is because the 0.32δ protrusion height fully captures the reversed region.

CHAPTER 4: BIO-INSPIRED SCALE ARRAYS IN TURBULENT BOUNDARY LAYER SEPARATION

4.1 INTRODUCTION

While the results from the laminar boundary layer experiments are promising, prior studies have shown that the mako shark skin is more effective at controlling separation in a turbulent boundary layer. The separation in a turbulent boundary layer is investigated with a flat plate, an array of smaller scales (scale size 1), and an array of larger scales (scale size 2). The three conditions are compared in a weak adverse pressure gradient case and a strong adverse pressure gradient case. The freestream velocity, Reynolds number and cylinder velocity ratio for each of the cases in this study are shown in Table 4.1.

Tunnel Velocity (m/s)	**Reynolds Number**	**α Weak APG**	**α Strong APG**
0.33	4.82×10^5	3.40	4.05
0.40	5.85×10^5	3.54	4.01
0.47	6.87×10^5	3.58	3.98

Table 4.1 TBL cylinder velocity ratios

Similar to Chapter 3, the reversing flow percentage plots will have the model location, boundary layer height, and the height of the scale at the maximum bristling angle (50°). The protrusion height for scale size 1 is 0.3 y/D and is 0.09 y/D for scale size 2. The boundary layer height for a zero-pressure gradient for each case is in Table 4.2.

Tunnel Velocity (m/s)	Reynolds Number	Boundary Layer Height (y/D)
0.33	4.82×10^5	0.79
0.40	5.85×10^5	0.77
0.47	6.87×10^5	0.74

Table 4.2 Boundary layer and protrusion heights for test cases

4.2 WEAK ADVERSE PRESSURE GRADIENT

Since the V3V system captures a volume of data and that data is separated into 44 separate planes, the plane perpendicular to the plate at the center of the scale model has been selected for 2D analysis. The system captures a total of 400 images in one run, so 26.67 s of data is recorded per run. For the backflow plots, four runs of data are time-averaged for a single set. The scale model is located between 28.6 and 28.8 x/D for the appropriate cases. The model is entirely contained within the measurement volume, so there should be uncontrolled backflow upstream of the model location, and if there is flow control, then it should be observed downstream of the model. Fig. 4.1 displays Case 1, the reversing flow percentage for the three conditions at Re = 4.82×10^5 and $\alpha = 3.40$.

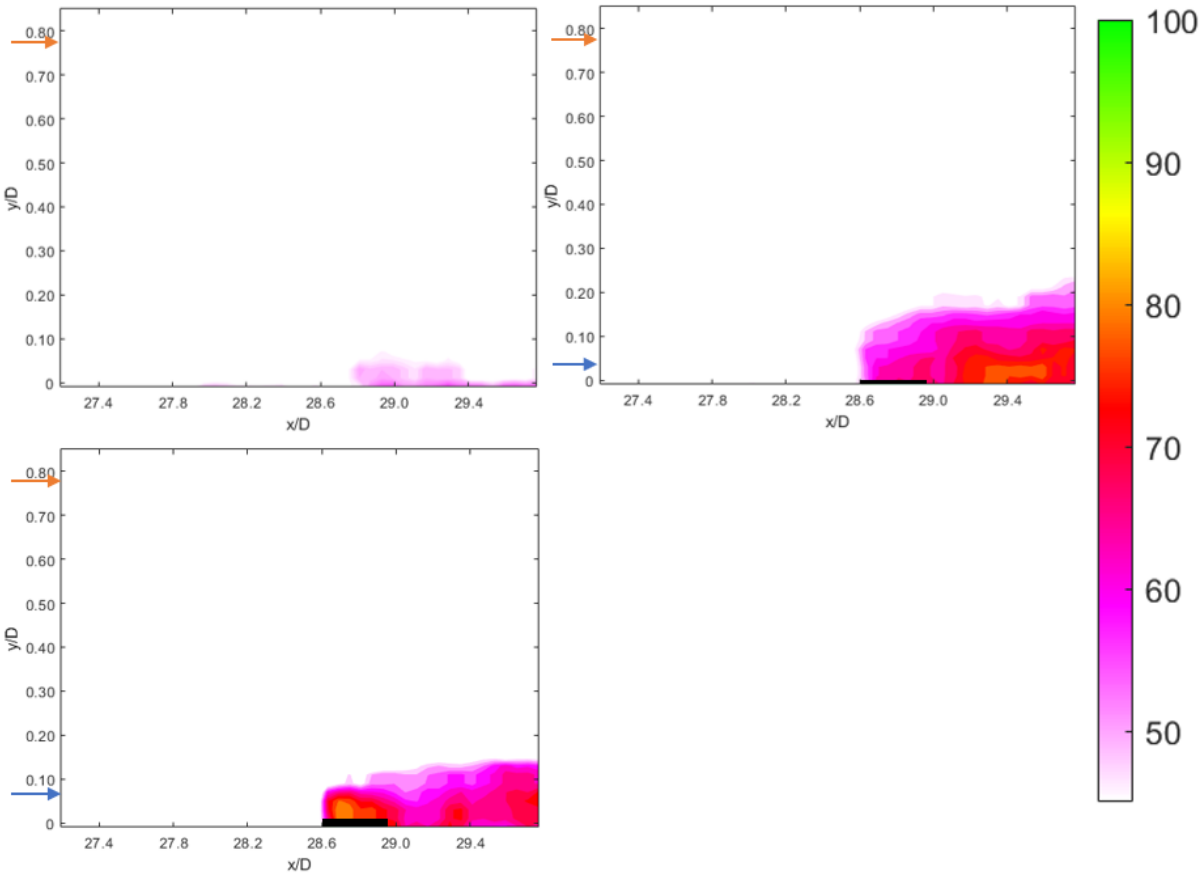

Figure 4.1 Weak APG backflow percentage: case 1. a) flat plate, b) scale 1, c) scale 2

There is little separation for the flat plate condition along the entire window. Due to this, it is unlikely the scales are bristling in the other two conditions. This is apparent by the fact that the scales significantly worsen the separation for the latter two conditions.

For case 2, the Reynolds number increases to Re = 5.85 x 10^5 and the cylinder velocity ratio increases to α = 3.54. The results of this case are shown in Fig. 4.2.

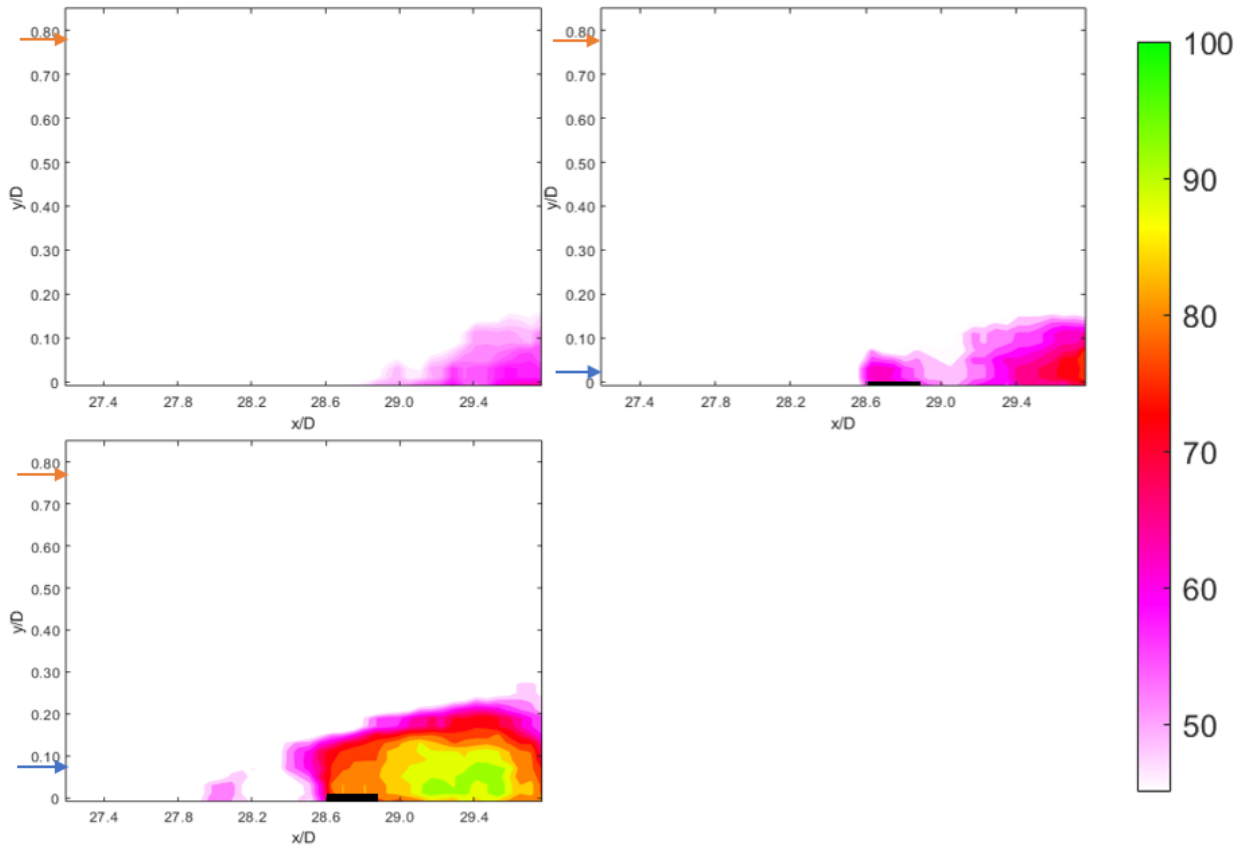

Figure 4.2 Weak APG backflow percentage: case 2. a) flat plate, b) scale 1, c) scale 2

For case 2, the separation is again fairly minimal for the flat plate case. Similar to case 1, scale size 2 in a flow with minor separation significantly worsened the flow downstream of the model. However, it appears that the smaller scale array has only minor negative effects on the flow, and it is improved relative to the same condition in case 1.

The final case for the weak adverse pressure gradient is case 3 with Re = 6.87 x 10^5 and α = 3.58. These results are shown in Fig. 4.3.

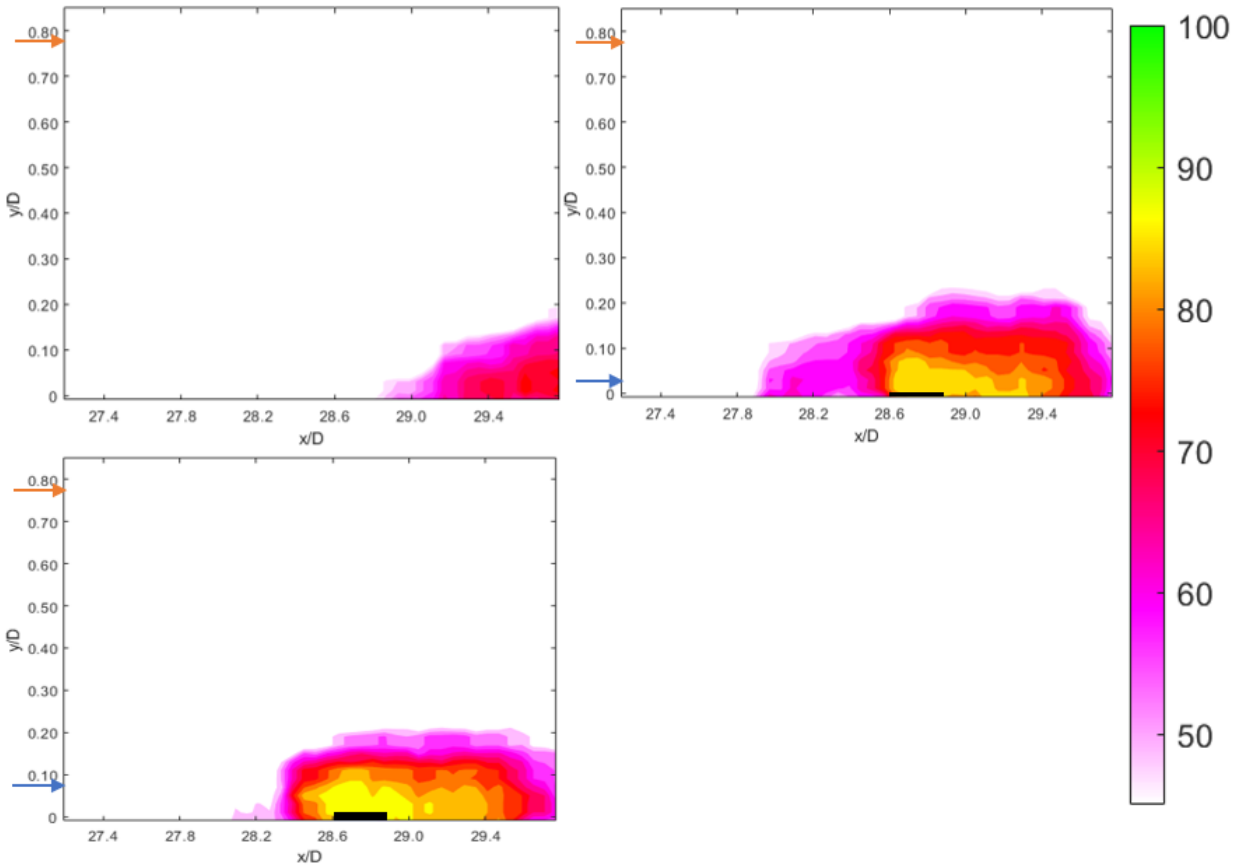

Figure 4.3 Weak APG backflow percentage: case 3. a) flat plate, b) scale 1, c) scale 2

Case 3 displays similar results to case 1 and case 2. The separation for the flat plate condition begins downstream of the scale models' location in the other two conditions, thus the scales cannot be bristled. The lack of bristling causes the flow separation to worsen for the conditions with the scale models.

4.3 STRONG ADVERSE PRESSURE GRADIENT

Building from the results of the previous section, the strength of the adverse pressure gradient significantly increases to produce very high separation. In the prior section, the flow is only just separated and the scale models are not effective in controlling the flow.

In this section, the flow is extremely separated to examine the difference in flow control effectiveness. The first case to be examined is case 4 with Re = 4.82 x 10^5 and α = 4.05.

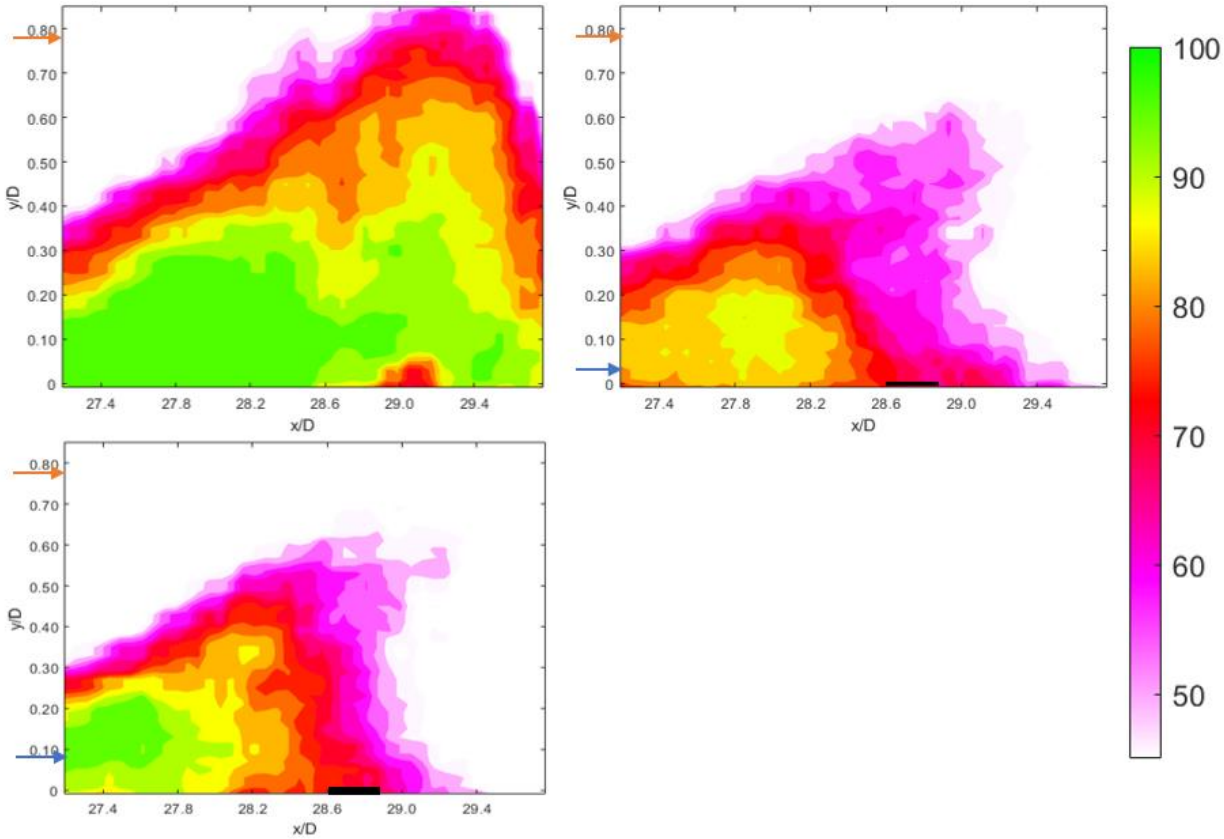

Figure 4.4 Strong APG backflow percentage: case 4. a) flat plate, b) scale 1, c) scale 2

In case 4, the flat plate condition displays highly separated flow with χ=1.0 (reversed flow 100% of the time) on the plate for 50% of the image. Additionally, there is no reattachment point and the height of the separation is at least 0.80 y/D. For the array of smaller scales, however, the backflow is significantly reduced across the entire image. There is no reattachment point, but the flow is barely separated downstream of the model (29.4 x/D). The height of the separation bubble has been reduced by at least 28%. For the array of larger scales, a degree of separation control is also demonstrated.

While scale size 1 eliminated areas of $\chi \geq 0.90$, scale size 2 has a visible reattachment point at 29.4 x/D and the separation bubble height has decreased by approximately the same amount as scale size 1 compared to the flat plate condition.

Case 5 matches the Reynolds number of Case 2, Re = 5.85 x 10^5, but increases α to α = 4.01. The results of this case are shown in Fig. 4.5.

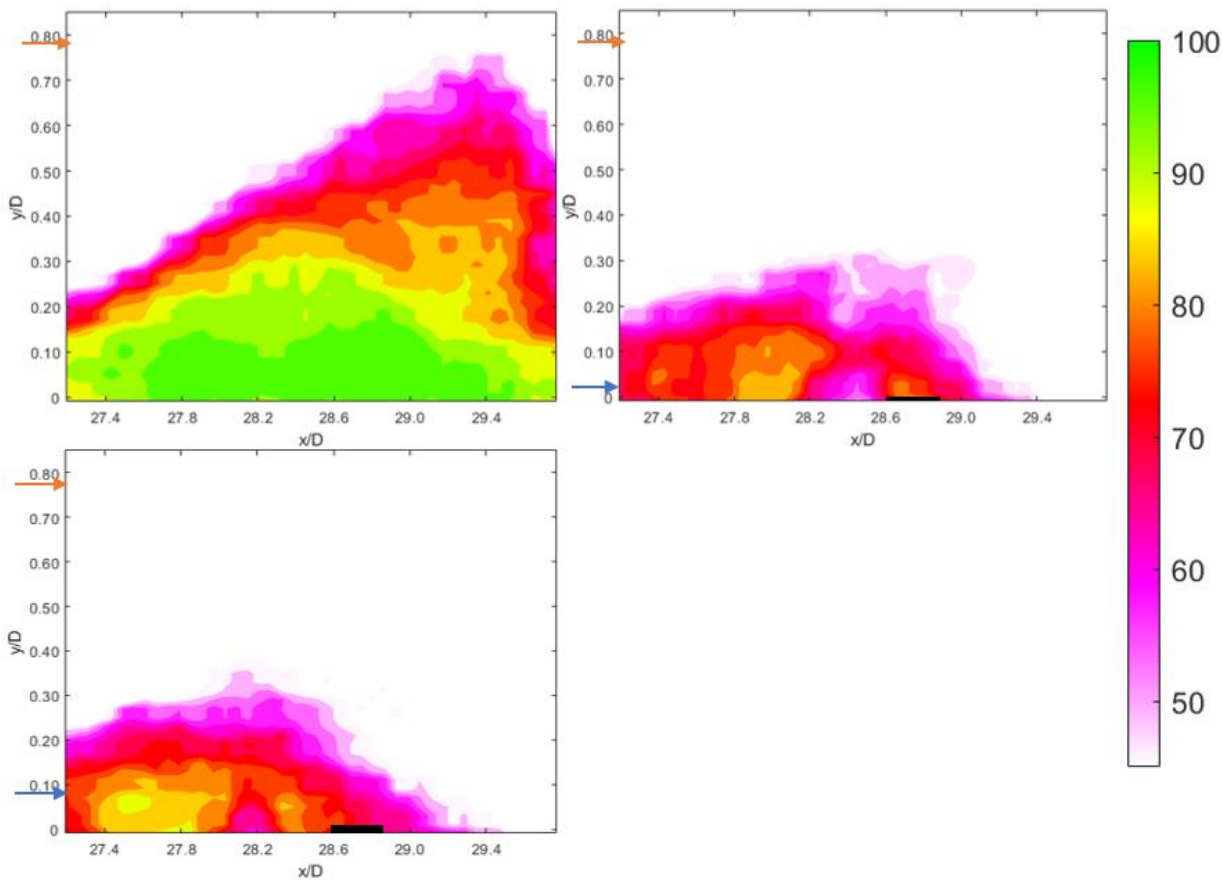

Figure 4.5 Strong APG backflow percentage: case 5. a) flat plate, b) scale 1, c) scale 2

The strong adverse pressure gradient in this case produces another highly separated flat plate condition, with $\chi \geq 0.90$ spanning the entire image from 27.4 x/D to 29.6 x/D. Additionally, the maximum height of the separation bubble is 0.75 y/D, so it is slightly smaller than the bubble present for case 4.

Both scale models produce similar results to one another. Each has a reattachment point near 29.4 x/D, but the smaller scale model reduces the separation bubble height by 64% and the larger model reduces the height by 57%.

The final case to be analyzed is case 6, with Re = 6.87 x 10^5 and α = 3.98. The results are displayed in Fig. 4.6.

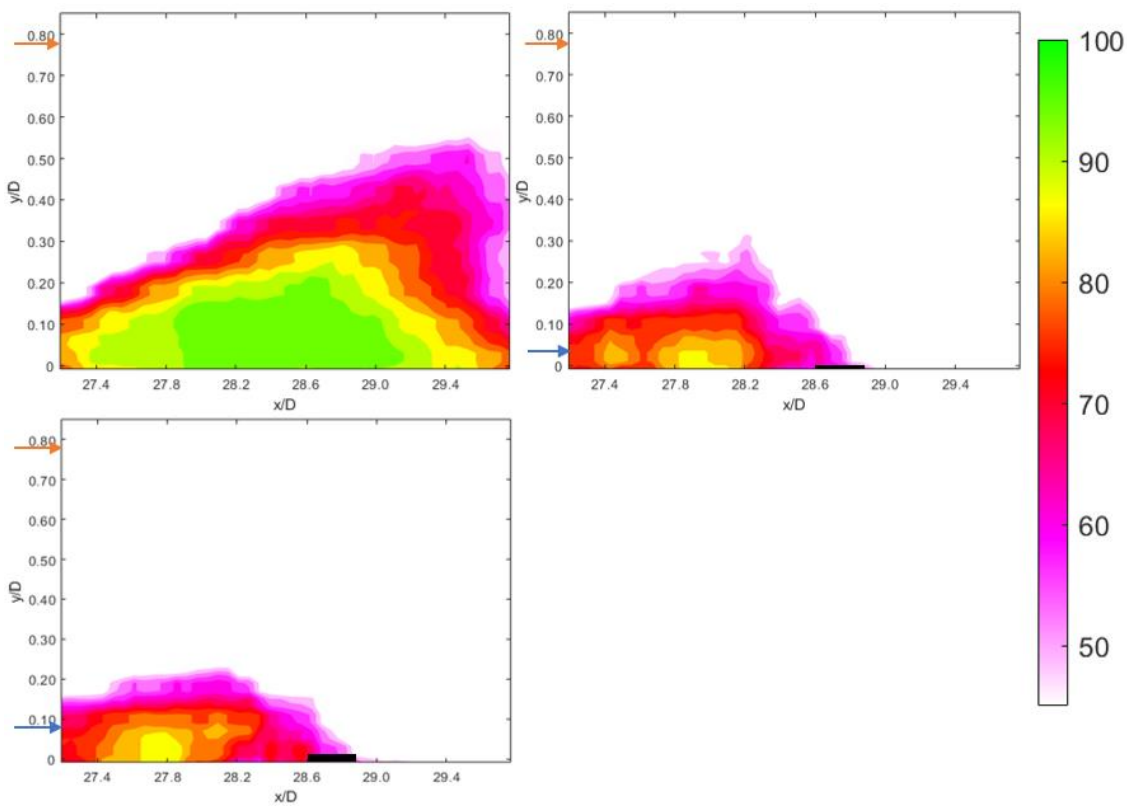

Figure 4.6 Strong APG backflow percentage: case 6. a) flat plate, b) scale 1, c) scale 2

Case 6 shows a highly separated flow for the flat plate condition, though it is less extreme than in case 4 or case 5. Regardless, it is ideal to eliminate that separation, which is accomplished by the scale models. The flow reattaches at 29.0 x/D, and the height of the separation bubble has been reduced by at least 50%. Although significant separation upstream of the scale models continues to exist, the models completely eliminate the separation downstream.

4.4 WEIGHTED BACKFLOW

A weighted area analysis is performed to better quantify the scale models effectiveness of reducing reversing flow. Each reversing flow plot for the weak and strong adverse pressure gradient conditions was split into a 44 x 44 grid. The area of each grid was multiplied by the backflow coefficient and summed. This grid size is the smallest that can be used since V3V separates the data into that number of planes. It is not the case in PIV data which is capable of a smaller grid element area. Thus, it is not viable to directly compare the weighted backflow coefficients for the laminar and turbulent boundary layer cases. However, it is used to compare the turbulent boundary layer cases. The weighted backflow coefficient (WBC) for all turbulent boundary layer cases are shown in Table 4.3.

	Weak APG				**Strong APG**			
Re	α	Flat Plate WBC	Scale Size 1 WBC	Scale Size 2 WBC	α	Flat Plate WBC	Scale Size 1 WBC	Scale Size 2 WBC
4.82×10^5	3.40	0.021	0.098	0.109	4.05	1.449	0.740	0.761
5.58×10^5	3.54	0.034	0.154	0.229	4.01	1.118	0.371	0.392
6.87×10^5	3.58	0.073	0.250	0.254	3.98	0.824	0.239	0.256

Table 4.3 Weighted backflow coefficient for TBL cases

The percentage change for each scale model when compared to the flat plate condition is shown in Table 4.4

	Weak APG			Strong APG		
Re	α	Scale Size 1 Change	Scale Size 2 Change	α	Scale Size 1 Change	Scale Size 2 Change
4.82 x 10^5	3.40	377%	433%	4.05	-48.9%	-47.5%
5.58 x 10^5	3.54	349%	569%	4.01	-66.8%	-65.0%
6.87 x 10^5	3.58	243%	252%	3.98	-71.0%	-69.1%

Table 4.4 Percent change in WBC for the scale models

Table 4.3 and Table 4.4 support the observations made for the reversing flow plots. When separation is not strong enough to bristle the scales, the models worsen the flow by increasing the total separation by up to 569%. However, in a suitably strong adverse pressure gradient, both sets of models successfully control the flow. The total reversing flow is reduced by up to 71%, including flow benefits upstream of the model location.

The WBC also allows for a better comparison between scale size 1 and scale size 2. In weak adverse pressure gradient conditions, the larger scale size 2 creates worse flow conditions compared to the smaller size due to the larger protrusion into the boundary layer. However, in the strong adverse pressure gradient, the two models perform comparably, with scale size 1 performing just 1.7% better on average.

4.5 TURBULENCE INTENSITY

To show the flow is indeed turbulent, the turbulence intensity for each flat plate case is calculated. Fig. 4.7 shows the turbulence intensity values at 28.7 x/D.

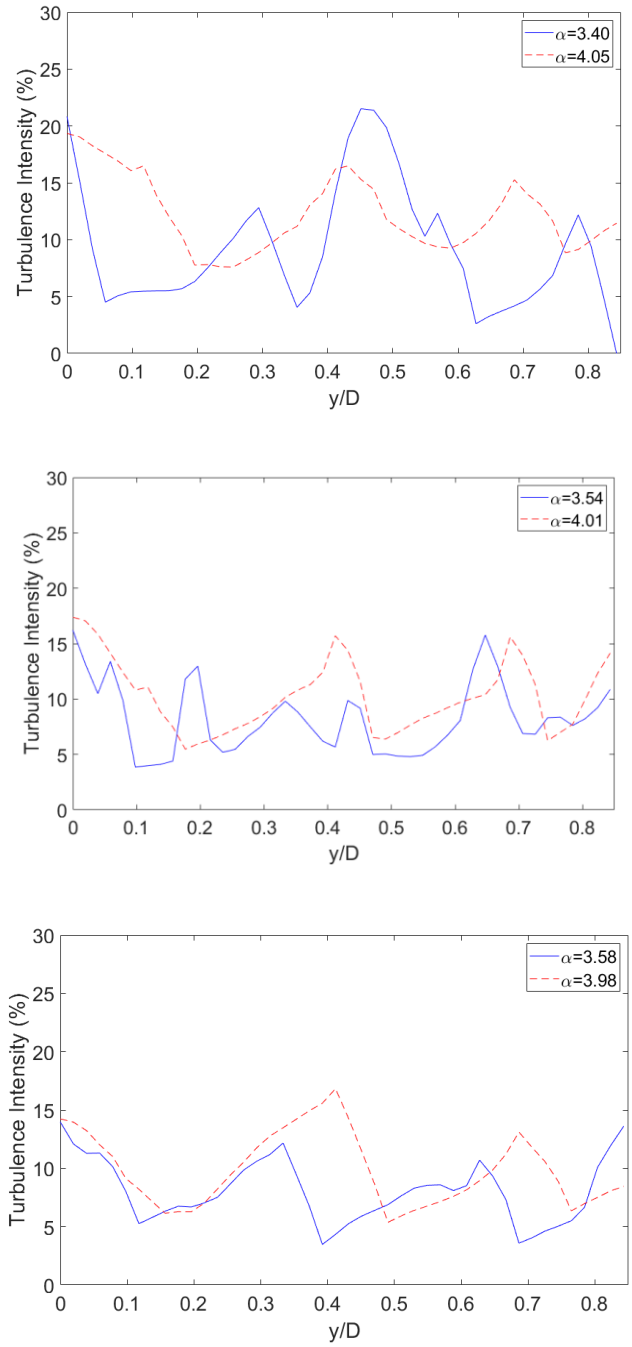

Figure 4.7 Turbulence intensity for TBL cases. a) Re = 4.82 x 10^5, b) Re = 5.85 x 10^5, c) Re = 6.87 x 10^5

For the weak adverse pressure gradient cases, the average turbulence intensity is 8.50 ± 4.73 and for the strong adverse pressure gradient cases, it is 10.85 ± 4.10, so the experiment is in high turbulence conditions [39]. The large standard deviation is an area of concern and can likely be explained by the V3V system. Since the V3V system is not resolved for small turbulent structures, the accuracy of the velocity fluctuations is questionable. The data planes that V3V utilizes and the low frame rate likely contribute to these fluctuations. For confirmation of the turbulence intensity levels, PIV data should be collected for each case and a greater quantity of images should be time averaged.

4.6 REYNOLDS STRESS

Evaluating the Reynolds stress for a turbulent boundary layer is a tool beneficial recognizing mixing and separation. The Reynolds stress is $-\rho\overline{u'v'}$ where u' and v' are velocity fluctuations. For the purposes of this study, the density term is dropped and $-\overline{u'v'}$ is non-dimensionalized by U^2. Case 6 is analyzed, and the plot is Fig. 4.8.

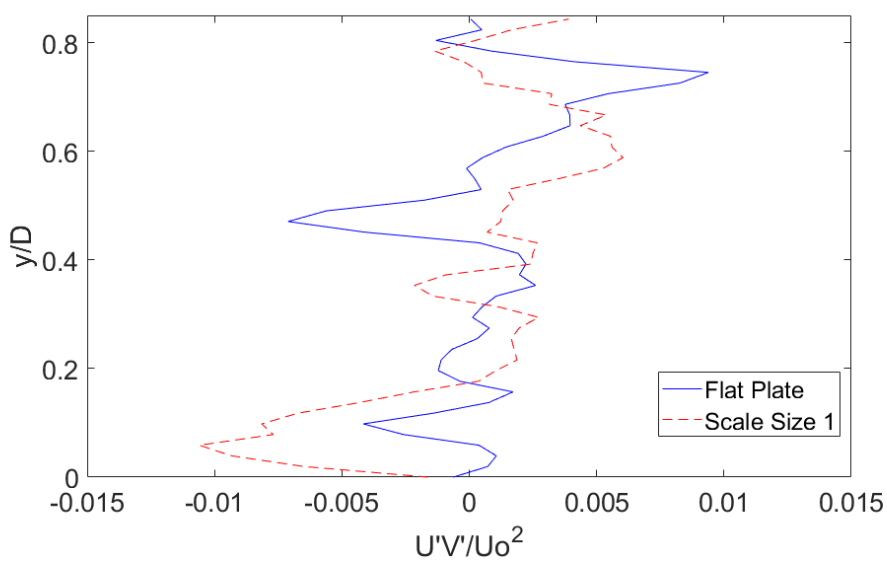

Figure 4.8 Reynolds stress for Re = 6.87 x 10^5 and α = 3.98 at 28.8 x/D

Fig. 4.8 shows the Reynolds stress at a single point (28.8 x/D). The selection of this point corresponds to the location just downstream of the scale array. As can be seen in Fig. 4.6, separation is present at this point for the flat plate condition but is not present for the scale size 1 condition.

In separated flows, the top of the separation bubble can be marked by a strong peak value in the magnitude of Reynolds shear stress [40]. This is apparent in the flat plate condition in Fig. 4.8 as there is a peak at 0.47 y/D, which is also the height of the separation bubble at this point. Another observation is the region of negative Reynolds shear stress close to the surface in the scale size 1 condition. Since separation is not present at this point, this is indicative of flow mixing. The data supports theories that shark skin may enhance mixing to control the flow [9,12].

4.7 ISOSURFACES

A benefit of using the V3V is the ability to easily view different frames of reference to better understand what is occurring on a 3-D level. A sample image taken from the flat plate condition for case 6 (Re = 6.87 x 10^5 and α = 3.98) is used for Fig. 9 – Fig. 11. In the figures, the red isosurface corresponds to U = 0.1 m/s, which is 21% the magnitude of the freestream velocity. Each figure is not time-averaged data, it is a single snapshot of the flow. Fig. 4.9 is the flat plate condition for case 6 and the plane is perpendicular to the plate. The isosurface data shown demonstrates the ability for further analysis to be completed regarding the 3-D separation bubble. Other images examined appear to show flow control of the 3-D separated region directly downstream of the scale assembly, but this analysis is incomplete not included in this work.

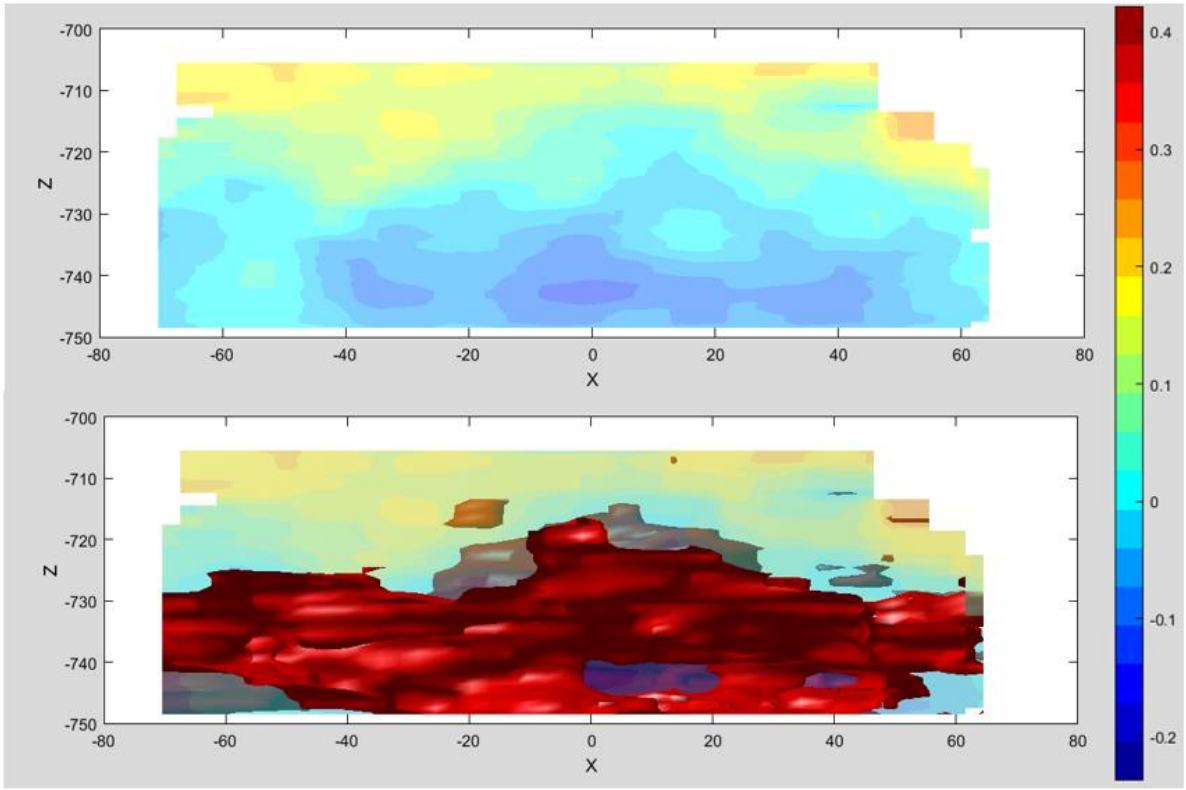

Figure 4.9 Flat plate case 6 velocity contour, perpendicular to plate

Fig. 4.9 shows a velocity contour plot both with and without isosurfaces. The isosurfaces show the extent of the large separation bubble. With V3V, the same image can be examined parallel to the plate, which is Fig. 4.10.

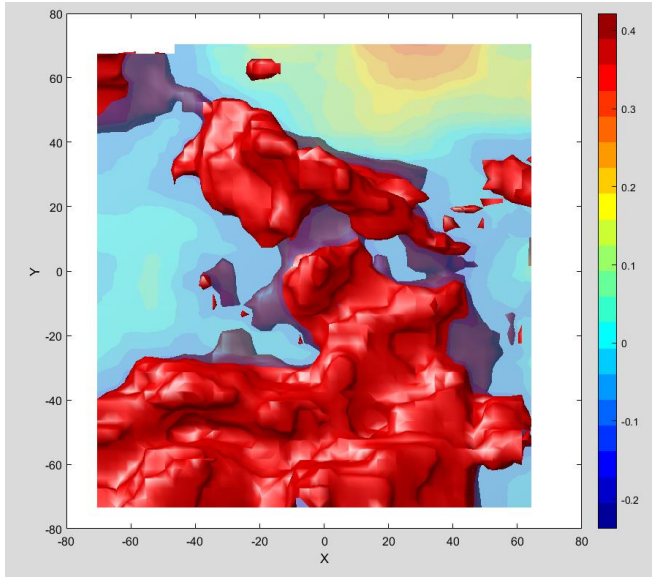

Figure 4.10 Flat plate case 6 velocity contour, parallel to plate

For Fig. 4.10, the plane shown is located at 0.1 y/D. The separation is occurring across the plate but is not constant in this image, so there are pockets of separation along the span of the plate. Fig. 4.11 shows a 3-D view of the separation bubble for the selected image.

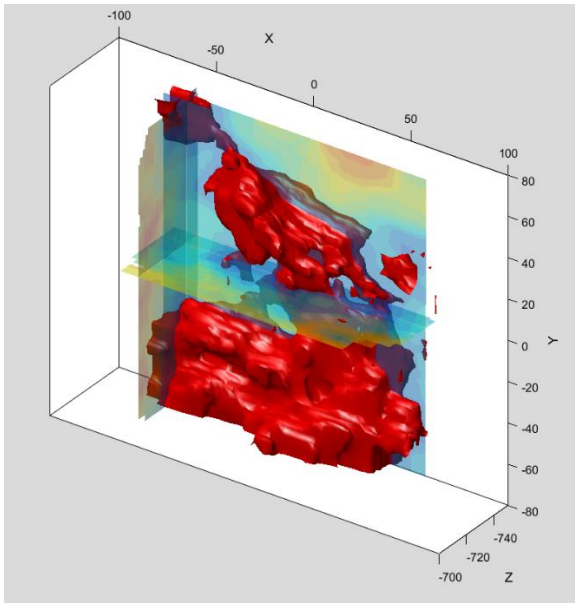

Figure 4.11 3-D view of the separation bubble

4.8 CONCLUSIONS

The results for the weak and strong adverse pressure gradient cases align with visual observation (no data shown) of the scale models in the tunnel. For the weak APG case, no bristling of the scales occurs, which can be attributed to the lack of strong reversing flow. As for the strong APG cases, sporadic bristling of the scales occurs. For the scale size 1 array, the all scales along a spanwise row do not bristle simultaneously, but rather bristled in small groups of two or three. Cases 1-3 with the weak adverse pressure gradient proved that the scales hinder flows with little separation. In the absence of strong reversed flow, the scales, unable to bristle, have a negative effect on the flow. This is visually confirmed to be the case, but no data exists for this observation. These findings conclude that the bio-inspired models cannot act as vortex generators as theorized on natural shark skin [21]. The current bio-inspired models used simply act as an obstacle in flows that are not highly separated.

Santos (2019) conducted a study regarding the width of low speed streaks in flow conditions matching the weak adverse pressure gradient cases used in the present study. The width of the low speed streak was observed to be at least 4.56 mm (for conditions matching case 1) [41]. This finding is wider than both scale models, so it is possible that this streak could bristle the scale models, even though the bristling was not observed.

When a strong adverse pressure gradient is utilized, as in cases 4-6, promising results are observed. The flat plate condition demonstrates a highly separated flow for each case with χ=1.0 commonly present. When the scale models are introduced to this highly separated flow, the scales demonstrate a strong degree of flow control.

The flow downstream of the scale arrays is successfully controlled by the bristling of the scales and the height of the separation bubble in general is vastly reduced by up to 70%. As expected, the location of the maximum separation bubble height moves upstream of the scale array instead of downstream of that location as in the flat plate case. Through the scales controlling the separation downstream of the array, this also leads to improvements upstream of the array. In each flat plate condition for all cases, the height of the separation bubble increases as x/D increases. This growth is eliminated when the array of scales is introduced, as the slope of the separation bubble is relatively flat. In addition to halting the growth, the height of the separation bubble upstream of the array is also reduced by an average of ~20%.

A weighted backflow coefficient is used to better quantify the differences between cases. This analysis finds that in the weak adverse pressure gradient, the scale models increase reversing flow by over 250% in all cases and up to 569%. This is contrasted by the results for the strong adverse pressure gradient, which finds reductions in reversing flow for all cases. The separation reduces by over 47.5% up to a 71.0% reduction for case 6. This analysis also finds that the performance difference between scale size 1 and scale size 2 is minimal, with scale size 1 performing just 1.7% better. The strong adverse pressure gradient concludes that bio-inspired scale models which dynamically bristle with reversing flow can act as an excellent method of passive flow control.

To prove the turbulent nature of the flow, the turbulence intensity is calculated for the three cases. Due to inherent issues with V3V data capture techniques, there are large fluctuations in turbulence intensity. However, this averages to a turbulence intensity of 10.85 ± 4.10 for the strong adverse pressure gradient case. Even though the standard deviation is large, the flow is highly turbulent regardless.

The Reynolds stress is calculated for case 6, comparing the flat plate condition to the scale size 1 condition. For the flat plate condition, a peak in Reynolds stress magnitude corresponds to the upper edge of the separation bubble. For the scale size 1 condition, a region of negative Reynolds stress is found which is indicative of mixing, a possible mechanism the scales use to control the flow.

Finally, an example of the uses of V3V is discussed. For a single image, planes parallel and perpendicular are examined and the separation bubble is visualized. The V3V system can be used by subsequent researchers to study 3-D vortex structures, separation bubble properties, low speed streaks, and more relevant investigations.

CHAPTER 5: SUMMARY AND CONCLUSIONS

Laminar and turbulent boundary layer separation control is the primary focus of this thesis. In a laminar boundary layer, a bio-inspired microflap model is successfully bristled passively by a vortex likely created by the interaction between flow instabilities sourced in the cylinder wake and instabilities from the microflap models impeding flow in the preferred direction. This study is the first known documentation of models passively bristling in a water tunnel that show passive flow control of boundary layer separation. The microflaps inhibit the clockwise rotational flow of the vortex, which bristles the model. Consequently, the integrity of the vortex structure is compromised and begins to break down. The results obtained are similar to observations that a backflow flap on an airfoil reduces the negative effects of dynamic stall by breaking down the DSV into two smaller vortices [24,25]. Two smaller time-averaged vortices occur in the flow, one upstream and one downstream of the microflaps. Due to the similarities to the DSV studies, further investigations using the bio-inspired models in unsteady cases, specifically in the interest of dynamic stall, should be conducted.

The reversing flow percentage for three cases is also calculated and plotted. The reversing flow upstream of the microflap models is still present, but the reversing flow downstream of the models is notably reduced. This reduction is quantified by the weighted backflow coefficient (WBC). The WBC multiplies the backflow coefficient by a non-dimensional differential area and sums the results for each test condition. This analysis finds that each microflap size successfully reduces the overall reversing flow, with the 0.40δ protrusion

height recording a 10.5% average reduction, the 0.32δ height reducing reversing flow by an average of 49.9%, and the smallest 0.25δ case reduces backflow by 40.7%. It is clear that the 0.40δ protrusion height microflap did not perform nearly as effectively as the other two sizes. This is possibly because the maximum bristling height for the microflap is greater than the original separation bubble height for the flat plate conditions. The two smaller microflap models are able to control separation effectively. The turbulence intensity for the three laminar boundary layer cases are all under 2%, thus confirming that the flow is laminar [39].

The importance of dynamic bristling is also noted. In the same flow conditions used for case 1-3 in the laminar boundary layer, the 0.25δ microflaps are observed when $\alpha = 2.02$. Since $\alpha > 2.0$, the cylinder wake will not affect the measurement window [34]. As a result, the vortex consistently seen in the other laminar boundary layer cases is not present. Without the vortex interacting with the microflaps, the models are static and suspended in a semi-bristled state within the laminar separation bubble. Without the dynamic motion, the microflap array increases the reversing flow by nearly 200% compared to the flat plate case [42].

The semi-static (~20° bristling angle) case is worthy of further analysis. The end goal for the bio-inspired models discussed in this study is to be utilized on aerodynamic and hydrodynamic bodies for separation control. In air, the semi-bristled static state is unlikely to occur since the density of air is much less than that of water. The semi-bristled state is likely due to a combination of the model orientation with respect to the water tunnel and the equilibrium state. The microflap has stationary fluid under the bottom surface of the microflap, which would not occur in air. Additionally, it may be more difficult to replicate the bristling motion as seen in this study in a wind tunnel. Since water has a higher density, the reversing flow velocity required to bristle the microflaps is likely significantly lower than the velocity required in air.

Compared to the study by Du Clos (2018), the present study finds a similar vortex formation on each side of the model as was present on the natural shark skin [12]. Du Clos also found that the natural scale bristling was sporadic and seemed randomly occur across the region. This is consistent with the visual observations of the scale models in the turbulent boundary layer experiment, but not with the microflaps in the laminar boundary layer.

For the turbulent boundary layer study, two arrays of bio-inspired scale models are tested in a weak and a strong adverse pressure gradient. In the weak adverse pressure gradient, the separation on the flat plate is not strong enough to bristle the scales, so the models prove to have a negative effect on the flow by increasing the separation by up to 569% compared to the flat plate case. As for the strong adverse pressure gradient case, extreme separation is present for the flat plate condition, but the models demonstrate excellent flow control by reducing the reversing flow by up to 71%. In addition, the models reduce the height of the separation bubble by 70% and the x/D location of this maximum separation height moves upstream from approximately 29.4 x/D for the flat plate case to 28.2 x/D for the scale model cases. For reference, the center of the scale models is located at 28.7 x/D, so the point of maximum separation height now occurs upstream of the model array. Reattachment of the flow is also observed when using the models in the strong adverse pressure gradient case. The reattachment point is located at 29.4 x/D for both the $\alpha = 4.05$ and $\alpha = 4.01$ cases. For the $\alpha = 3.98$ case, reattachment occurs immediately downstream of the model location at 29.0 x/D.

Afroz (2014) hypothesized that the natural shark scales may be too small to enhance mixing near the surface [33]. The study found that the shark skin exhibited flow control in both laminar and turbulent boundary layer cases, as the present study also demonstrates. Afroz theorized that the primary mechanism of flow control may be the inhibition of reversing flow

and not necessarily the mixing of momentum near the surface. This may be the case for natural shark skin, but for the turbulent boundary layer cases in this study, it is unknown which phenomenon is affecting the flow more.

The scale models inhibit the reversing flow in the extreme separation conditions and redirect the flow to the preferred direction. However, there is evidence that the mixing of momentum is also occurring in the extreme separation conditions. The Reynolds stress for case 6 is calculated and plotted at 28.8 x/D, a location just downstream of the scale model array. This analysis finds a region 0.2 y/D in height of negative Reynolds stress, which is indicative of mixing [40]. For the Reynolds stress to be negative, there must be a sign change between the u and v velocity fluctuations. Since there is no reversing flow at this point, this indicates a large region of negative v velocity.

The studies find that the separation control effectiveness is somewhat dependent on protrusion height of the model into the boundary layer. For the turbulent flow cases, the difference between the two model sizes is fairly negligible, with only an average 1.7% difference in separation control effectiveness. As for the laminar flow cases, the model with the largest protrusion height (0.40δ) is the least effective and the middle protrusion height (0.32δ) is ~9% more effective than the smallest height (0.24δ) at controlling the reversing flow. This could be related to the fact that the maximum height of the reversed flow region is 0.28δ, so it is possible that the smallest protrusion height's inability to fully capture the separated region causes reduced effectiveness. The largest protrusion height fully captures the separated region but may interfere with the non-separated region enough to negate most of the benefits of capturing the separated region. The middle protrusion height may be a balance between fully capturing the reversing region and not too large for negative impacts on the non-reversed regions of the flow.

Neither scale model size tested is effective in reducing separation in the weak adverse pressure gradient conditions in a turbulent boundary layer even though the low speed streaks are wider than the width of the scale models, so scale bristling could theoretically occur [41].

It is possible that this low speed streak is not strong enough to bristle the scale models. In the same conditions, natural shark skin effectively controlled reversing flow [41], but this did not translate to the scale models. It is possible the low speed streaks are strong enough to bristle the natural shark skin but not the manufactured models in the current study.

Due to insignificant variances between the two scale sizes, it is likely that for a highly separated flow, the scale size is not a critical factor. It is probable that in these conditions, the important factor is the scales bristling and inhibiting the reversing flow, diminishing the importance of the boundary layer protrusion height. Damping or other parameters that may govern scale flexibility do not seem to be important. The goal for the model design used in this study is to maximize the likelihood of the scale bristling and responding to flow conditions by actuating, which is proven.

REFERENCES

1. Bushnell, D.M., and Moore, K.J., "Drag reduction in nature," *Annual Review of Fluid Mechanics*, Vol. 23, No. 1, 1991, pp. 65-79.

2. Simpson, R.L., "Turbulent boundary-layer separation," *Annual Review of Fluid Mechanics*, Vol. 21, No. 1, 1989, pp. 205-232.

3. Gustavsson, J., "Turbulent flow separation," thesis, Dept. Mechanics, Royal Institute of Technology, Stockholm. 2011.

4. Meyer R., Bechert D.W., Hage W, "Wind tunnel experiments with artificial bird feathers for passive separation control on airfoils," *Fluid Mechanics and its Applications*, Vol. 53, 1999.

5. Griffin, R., "Design of passive flow control device derived from bird wing aerodynamics," thesis, Tufts University, Dept. of Mechanical Engineering, 2017.

6. Sangha, G., "Aerodynamics of butterfly flight," thesis, Huddersfield Univ., Dept. of Mechanical Engineering, 2017.

7. Fish, F.E., "Imaginative solutions by marine organisms for drag reduction," *Proceedings of the International Symposium on Seawater Drag Reduction*, 1998.

8. Fish, F.E. "Passive and active flow control by swimming fishes and mammals," *Annu. Rev. Fluid Mech.*, Vol. 38, 2006, 193-224.

9. Lang, A., Motta, P., Hidalgo, P., "Bristled shark skin: a microgeometry for boundary layer control?," *Bioinspiration & biomimetics*, Vol. 3, No. 4, 2008.

10. Lang, A., Motta, P., Habegger, M.L., Hueter, R., "Shark skin boundary layer control," *Natural Locomotion in Fluids and on* Surfaces, The IMA Volumes in Mathematics and its Applications, Vol. 155, 2011.

11. Domel, A.G., *et. al.*, "Shark skin-inspired designs that improve aerodynamic performance," *J. R. Soc. Interface, Vol. 15,* 2018.

12. Du Clos, K.T., Lang, A., Devey, S., Motta, P.J., Habegger, M.L., and Gemmell, B.J., "Passive bristling of mako shark scales in reversing flows," *J. R. Soc.* Interface, Vol. 15, 2018.

13. Raschi, W. & Tabit, C. 1992. "Functional aspects of placoid scales: A review and update. *Aust J Mar Fresh Res.* 43:123-147.

14. Lang A., Habegger M.L., Motta P., "Shark skin drag reduction," *Encyclopedia of Nanotechnology*, Springer, Dordrecht., 2015.15. Motta, P., Habegger, M.L., Lang, A., Hueter, R., Davis, J., "Scale morphology and flexibility in the shortfin mako Isurus oxyrinchus and the blacktip shark Carcharhinus limbatus," *Journal of Morphology*, Vol. 273, No. 10, 2012, pp. 1096-1110.

16. Graham, J.B., DeWar, H., Lai, N.C., Lowell, W.R., and Arce, S.M., "Aspects of shark swimming performance determined using a large water tunnel," *Journal of Experimental Biology*, Vol. 151, No. 1, 1990, pp. 175-192.

17. Brunnschweiler, J.M., "Water-escape velocities in jumping blacktip sharks," *Journal of the Royal Society Interface*, Vol. 2, No. 4, 2005, pp. 389-391.

18. Lang, A., Motta, P., Habegger, M. L., Hueter, R., Afroz, F., "Shark skin separation control mechanisms," *Marine Technology Society Journal*, Vol. 45, No. 4, 2011, pp. 208-215.

19. Bechert, D.W., Bartenwerfer, M., Hoppe, G., and Reif, W.E., "Drag reduction mechanisms derived from shark skin," ICAS conference proceedings, 1986, pp. 1044-1068.

20. Bechert, D.W., Bruse, M., Hage, W., and Van der Hoeven, J.G., "Experiments on drag-reducing surfaces and their optimization with an adjustable geometry," Cambridge University Press, 1997.

21. Bechert, D.W, "Experiments with three-dimensional riblets as an idealized model of shark skin" 2000.

22. Dean, B., and Bhushan, B., "Shark-skin surfaces for fluid-drag reduction in turbulent flow: a review," 2010.

23. Lin, J.C., "Review of research on low-profile vortex generators to control boundary-layer separation," *Progress in Aerospace Sciences*, Vol. 38, 2002, pp. 389-420.

24. Gardner, A.D., Opitz, S., Wolf, C.C., and Merz, C.B., "Reduction of dynamic stall using a back-flow flap," *CEAS Aeronautical Journal*, Vol. 8, 2017, pp. 271-286.

25. Wolf, C.C., Gardner, A.D., Merz, C.B., and Opitz, S., "Influence of a back-flow flap on the dynamic stall flow topology," *CEAS Aeronautical Journal*, Vol. 9, 2018, pp. 39-51.

26. Jung, Y.C., and Bhushan, B., "Biomimetic structures for fluid drag reduction in laminar and turbulent flows," *Journal of Physics: Condensed Matter*, Vol. 22, No. 3, 2009.

27. Domel, A.G., Saadat, M., Weaver, J.C., *et. al.*, "Shark skin-inspired designs that improve aerodynamic performance," *Journal of the Royal Society Interface*, Vol. 15, No. 139, 2018.

28. Evans, H.B., Hamed, A.M., Gorumlu, S., Doosttalab, A., Aksak, B., Chamorro, L.P., and Castillo, L., "Engineered bio-inspired coating for passive flow control," *Proceedings of the National Academy of Sciences of the United States of America*, Vol. 115, No. 6, 2018, pp. 1210-1214.

29. Wheelus, J., "An investigation of the flow control mechanisms of shorfin mako skin," thesis, Dept. of Aerospace Engineering and Mechanics, Univ. of Alabama, 2015.

30. Morris, J.A., "Application of shark skin flow control techniques to airflow," thesis, Dept. of Aerospace Engineering and Mechanics, Univ. of Alabama, 2017.

31. Smith, D., "Turbulent separation control effects of mako shark skin samples on a NACA 4412 Hydrofoil," thesis, Dept. of Aerospace Engineering and Mechanics, Univ. of Alabama, 2011.

32. Bradshaw, M., "Laminar separation control effects of shortfin mako shark skin," thesis, Dept. of Aerospace Engineering and Mechanics, Univ. of Alabama, 2014.

33. Afroz, F., "Laminar and turbulent boundary layer separation control of mako shark skin," dissertation, Dept. of Aerospace Engineering and Mechanics, Univ. of Alabama, 2014.

34. Lam, K.M., "Vortex shedding flow behind a slowly rotating circular cylinder," *Journal of Fluids and Structures*, Vol. 25, 2009, pp.245-262.

35. Fage, A., and Preston, J.H., "On transition from laminar to turbulent flow in the boundary layer," *Royal Society Publishing*, 1941.

36. Willert, C., and Gharib, M., "Digital particle image velocimetry," *Experimental Fluids*, Vol. 10, 1991, pp. 181-193.

37. White, F. M., *Viscous Fluid Flow*, 2nd ed., McGraw-Hill Inc., 1991.

38. Stellmacher, M., Obermayer, K., "A new particle tracking algorithm based on deterministic annealing and alternative distance measures," *Experiments in Fluids*, Vol. 28, 2000, pp. 506-516.

39. Vanoni, V.A. and Brooks, N.H., "A study of turbulence and diffusion using tracers in a water tunnel," Department of the Air Force, Report No. E-46, 1955.

40. Patrick, W.P., "Flowfield measurements in a separated and reattached flat plate turbulent boundary layer," NASA Contractor Report 4052, 1987.

41. Santos, L., "Low speed streaks as triggers for passive bristling of shark scales for turbulent boundary layer separation control," APS DFD 72nd Annual Meeting, 2019.

42. Parsons, J.C., "Actuation of passive flaps modeled after shark scales in a steady laminar boundary layer," APS DFD 71st Annual Meeting, 2018.